Journal of Materials Sciences and Applications
2020; 6(1): 1-23
http://www.aascit.org/journal/jmsa
ISSN: 2381-0998 (Print); ISSN: 2381-1005 (Online)

American Association for Science and Technology

Electropositive Promotion of DC HF CCVD Synthesis of Carbon Nanotubes: A Review

Jeannot Mane Mane[1, 2, 3, *], Nyangono Kouma Jean Michel[2], Bridinette Thiodjio Sendja[1]

[1]Department of Mathematics and Physical Sciences, Ecole Nationale Supérieure Polytechnique (National Advanced School of Engineering), University of Yaoundé I, Yaoundé, Cameroon

[2]Basical Scientific Teachings (ESB) Department, Advanced Teachers' Training College for Technical Education (ENSET), University of Douala, Douala, Cameroon

[3]Departement of Physics, Faculty of Sciences, University of Dschang, Dschang, Cameroon

Email address

Jeannotmane@yahoo.fr (J. M. Mane)

[*]Corresponding author

Citation

Jeannot Mane Mane, Nyangono Kouma Jean Michel, Bridinette Thiodjio Sendja. Electropositive Promotion of DC HF CCVD Synthesis of Carbon Nanotubes: A Review. *Journal of Materials Sciences and Applications*. Vol. 6, No. 1, 2020, pp. 1-23.

Received: April 11, 2020; **Accepted**: June 22, 2020; **Published**: November 26, 2020

Abstract: Ability of electropositive element atoms to promote catalysis by transition metal atoms of carbon nanotubes growth by CVD process, the so called DC HF CCVD is concerned. The starting point and originality is promotion of adsorption of ethylene on transition metal dense face surfaces (Pt(111)) in presence of substrate surface pre-covered with alkali atoms. Promoting effect then being sketched by conversion of adsorption mode from a di-σ type bonding on the bare substrate surface to a π-bonding mode in the presence of pre-covered promotor's atoms and at their adsorption site vicinity. This promoting behavior induces molecular orbitals positions shifts with increasing alkali coverage as evidenced in UPS and XPS line position changes and variations in relative adsorbed amounts of each species of alkyne as shown by TDS. Results have been understood within theoretical electrostatic models and charge transfer between TM-substrate and promoting atoms, and between promotor and alkyne through the Chatt-Duncanson model. Assuming catalysis of CVD growth process of CNTs by TM particles pre-coverage of a substrate of SiO_2/Si(100), the obtained CNTs may be considered to be bonded to TM catalyst spread inside the tubes in a bonding state referred to as STATE1. This supposes top growth mode through VLS mechanism, initiated by pop-corn like lift of catalyst particles under increase of temperature. Growth carried under these conditions leads to nanotubes with a certain size and length distribution. While pre-covering catalyst clusters with alkali atoms prior to CVD process, this would favor interaction between catalyst and promotor first, inducing strong charge transfer from alkali towards TM particle, thus weakening the next interaction between the synthetized nanotube and resulting «promoted catalyst». Obtained nanotube structure in a bonding state referred to as STATE2 would be more weakly bonded to the «catalyst», compared to STATE1. As well, overall CNTs height should then be a beet shortened compared to the first case. Expected experimental results may be checked through DCD model and vibrational spectroscopies through the eventual shift of band transitions occurring. The same may be done in XPS for s-resonance line position shifts. Expected is easier release of catalyst particles in the course of CNTs purification aiming specific applications such as hydrogen storage. The work may have some implications in device implementation implicating CNTs defects. Experimental applications may follow.

Keywords: Carbon Nanotubes, Promotion of DC HF CCVD of CNTs, Charge Transfer Promotor-TM and TM-C, DCD Model, Electrostatic Models, Defects

1. General Introduction

Carbon nanotubes (CNTs) have attracted an enormous interest since their first report in 1991 [1] due to their outstanding properties. Their highly anisotropic form suggests they may be considered as nearly 1D nanomaterials. Hence a special attention has been devoted to the electron field emission from CNTs. In this specific case, the very high aspect ratio is expected to markedly decrease the emission threshold at the tip of the nanotube. This field emission property as well

as many others such as a high aspect ratio, a reasonable work function, chemical inertness and mechanical robustness provide them related applications and make them very interesting on a technological point of view. Preparation of such samples implies the growth of bundles or individual aligned nanotubes standing on flat substrate. Catalytic Chemical Vapour Deposition (CCVD) techniques using plasma-enhancement (PE-CCVD) and direct current and hot filaments (DC HF CCVD) have proven to be the best suited to fulfil these requirements as the local electric field orientates the growth normal to the surface. Thus a fine and localized control of the nucleation and growth of oriented nanotubes can be achieved from catalyst made up of transition metal particles (Fe, Co, Ni) spread onto the surface [2]. From the many studies devoted to that important field emission property, it has been concluded that the CNTs must be i) well aligned, but ii) with a scarce and regular density in order to prevent the screening of field emission by the nanotubes just in the vicinity [3]. On films grown by (PE CCVD) processes, the role of the electric field is underlined with a reported threshold for alignment [4].

A recent paper [5] described some phenomena that may occur at the level of the half fullerene cap with transition metal (TM) catalyst capped on top of the CNT: curvature induced carbon atoms rehybridization and occurrence of defects (topological, vacancies, dislocations), contamination, charge transfer between the transition metal and carbon atoms. This charge transfer has been cited in a recent pass and, proved by X-ray Absorption Spectroscopy (XAS) and Scanning Photoelectron Microscopy (SPEM), to be responsible of UDOS (Unoccupied Density of States) changes at the vicinity of the Fermi level and would influence the absorption transitions [6]. Hence, charge transfer may contribute to the modification of the electronic structure of CNTs tips. Indeed, XANES detects the transitions from core electrons to the conduction band of the solid, providing an image of the density of unoccupied states (UNDOS). XANES therefore provides structural and electronical information about atoms, molecules and chemical functionalities in the medium range order. This property of XANES is due to the angular dependence of the absorption transitions [7]. This angular dependence had been reported on graphite since a long time [7] and the analysis has been further refined both on an experimental and a theoretical points of view [8, 9]. XANES is a local probe sensitive to chemical impurities, defects, chemical adsorption and curvature-induced orbital rehybridization.

X-ray absorption spectroscopy (XAS) recorded on the carbon K-edge is a powerful tool to provide chemically-selective information on the local environment around carbon in solid materials, like CVD diamond [8, 9, 10, 11], amorphous carbon nitride [8, 12], amorphous graphitic carbon [8, 10] and CNTs [8, 13, 14, 15]. Accordingly this local probe would be sensitive to chemical impurities, defects, chemical adsorption, curvature-induced orbital rehybridization and defects, charge transfer and others. Previous papers have been reported on the angular dependence at the C K edge from carbon nanostructures films grown by different CVD methods [8, 9, 16, 17].

The paper [5] studied the charge transfer between the TM and carbon atoms (TM-C) at the tips of carbon nanotubes (CNTs) grown on plain substrates in a mean direction normal to the surface by a DC HF CCVD process with transition metal (TM) catalyst capped on top of the CNT (top growth mode). The effect of the CNT curvature was underlined since it induces defects. The article aimed to tackle characterizing the nature of charge transfer between TM catalyst and carbon atoms at the level of the tips, thus allowing to discriminate between sp^2 and sp^3 hybridized carbon atoms, using the $\pi\sigma$ parameters retrieved from the so called Dewar-Chatt-Duncanson model [5, 18, 19, 20, 21, 22] and complementary vibrational spectra data on these CNTs [13, 23]; the cap being modelled as half a fullerene. This degree of rehybridization being in relation with the charge transfer. Since previous studies reached the conclusion that CNT grapheme carbon atoms along the side walls shells are essentially sp^2 hybridized, the effects of defects (topological, rehybridization, vacancies, dislocations, impurities and others) at the level of the cap may be underlined, due to the surface curvature effect. But, SEM and TEM analysis show that an amount of TM particles are smeared along the internal side wall shells of the tubes. The types of defects were discussed. The presence of non-hexagonal shaped carbon rings consists in topological defects which are localized mainly at tube ends and near tube bending zones. Their contamination and rehybridization are intrinsically related to the curvature of their graphene layers and may influence TM-C charge transfer.

The results point to $\pi\sigma$ parameter values retrieved from vibrational spectra measurements through the DCD model within the range of sp^2 hybridization of carbon atoms ($\pi\sigma \leq 0.4$). Meanwhile, through retrodonation from metal to carbon (or π-backdonation), charge is transferred back to tip carbons in the graphene matrix. The later in case the retrodonation becomes more important than forward donation (σ-donation) may enhance the DOS of unfilled states of tip carbons around the Fermi level. Then, by mastering the majority direction of this charge transfer TM-C, thus mastering the capability to willingly orientate this charge transfer direction may have some implications in the defect engineering through the judicious choice of the TM catalyst to be used for the PE HF CCVD synthesis of the carbon nanotubes [9, 24].

The present paper deals with the ability of electropositive elements (K, Cs) atoms to promote the catalysis by transition metal atoms (Co, Fe, Ni) of carbon nanotubes growth by a CVD process on SiO_2/Si(100) substrates, the so called classical DC HF CCVD. Such CNTs are aligned almost vertically on the substrate and are useful for field emission purposes. The interaction of electropositive alkali atoms with TM particles prior to the CVD process results in a first charge transfer dominated by the TM which is more electronegative, thus lowering the amount of charge density in the mixed catalyst formed, charge that could otherwise be able to strongly further interact with, and be back-donated to the alkyne C atoms during and after the CVD process. This alkali-TM interaction is described within electrostatic models

[25, 26]. This should lead to improving the quality of the CNTs performances. It is expected the length (height) of the obtained CNTs be somewhat reduced, compared to the case of catalysis by bare TM particles, while considering a pop-corn model for lifting the catalyst particles by thermal agitation.

After a shortened survey of the literature on carbon, graphite, fullerenes and carbon nanotubes where are described their main forms, characteristics and properties (physical, mechanical and electronic) in section 2. In section 3 is recalled the DCD model used so far for the characterization of charge transfer TM-Carbon in CCVD CNT fullerene cap region, by use of the πσ parameters extracted from HREELS (vibrational spectra) measurements and EELS (Electron Energy Loss Spectroscopy) [5, 23] on CNTs. Section 4 deals with: the classical DC HF CCVD mechanism including substrate preparation, the CVD process; the CNTs characterization by microscopic and spectroscopic methods; and the results retrieved from morphological and structural characterization by SEM and TEM, and vibrational spectra analysis to ascertain charge transfer TM-C through πσ parameter values. Section 5 presents a discussion of the results obtained and the conclusions derived. Section 6 deals with the effect of K and Cs atoms on ethylene adsorption on the Pt(111) surface. It analyses the interaction of alkali atoms with TM substrates and adsorption of alkynes on resulting surfaces. DCD and electrostatic models are concerned for interpretations. It explores the possibility to promote the classical DC HF CCVD by pre-coverage of TM particles by alkali atoms in the submonolayer regime prior to the CDV process. It discusses the lowering of charge transfer TM-C in the presence of TM pre-covered with alkali atoms. The paper ends by a short conclusion discussion in section 7 and experimental perspectives.

2. Literature Survey on Carbon, Carbon Graphite, Fullerenes and Carbon Nanotubes

2.1. Introduction

Carbon materials may be divided in two main groups of forms, the first is known as Traditional forms of carbon, including diamond (and lonsdaleite at some extent), graphite, carbynes and amorphous carbons; and the second is known to be Novel forms or Carbon Nanostructures (CNSs), including fullerenes, Carbon Nanotubes (CNTs), Carbon Nanofibers (CNFs), Carbon Nanowires (CNWs), Carbon nanowalls (CNWs) and Carbon Nanoparticles. Novel carbon-based materials reveal a variety of structures with a great deal of physical and chemical properties [1, 27 Krot85]. These unique ranges of properties [28] result from the reduced dimensionality, inherent to carbon containing nanosystems. They are susceptible of a wide range of applications [24, 28]. These new forms of carbon are emerging as the main target of many researchers around the world in pursuing nanoscale devices of the future [24, 28, 29].

As a consequence of this specific dimensional particularity, every nanostructure synthesized has to be characterized for fully mastering its proprieties and by the way, handling its applications [15, 28]. Besides fullerenes [30] and CNTs [1], there is nowadays, a plethora of carbon nanostructures. Among these novel nanostructures, carbon nanotube exhibits unique physical and chemical properties. It is promising to revolutionize several fields of fundamental *science* and contribute as major component of *nanotechnology*. It can be used in *composite materials* or in *individual functional element of nanodevices* such as: *hydrogen storage*, *nanomanipulation*, *medical usages* and *nanoporous membranes*.

This section provides information in the versatility of carbon element, allowing it to form more than 50% of known chemical compounds. Chemical vapour deposition (CVD) technique on a flat substrate [30] has become the most popular technique of CNTs synthesis and can lead to controlled growth of the CNTs by varying operating parameters such as gas mixture, temperature, pressure and catalyst.

2.2. Carbon Hybridization

Neutral carbon atom is divalent since it has totally six electrons with four of them occupying the outer orbit, two of them being unpaired. Therefore, the electronic configuration of the carbon atom at fundamental state is $1s^2 2s^2 2p_x^1 2p_y^1 2p_z^0$ and does not explain several bonds of carbon structures. It should in regard of this configuration form two covalent bonds. In reality, there are many compounds where carbon is tetravalent, like methane (CH_4). The formation of these materials with tetravalent carbon is due to the ability of carbon to hybridize, and allows it to be the most versatile element. Hybridization is a passage of the atom from one fundamental state to an excited state ($C^* 1s^2 2s^1 2p^3$), thus very reactive.

*2.2.1. Passage to an Excited Configuration Denoted C**

One electron of the 2s atomic orbital passes to the 2p atomic orbital, resulting in the $2s^1 2p^3$ electronic configuration. Thus offering the possibility to form four (4) bonds with carbon, but these bonds are not equivalent since they involve either one s electron or p electrons. The energy necessary to excite the carbon atom (passage from the fundamental configuration $2s^2 2p^2$ to the excited configuration $2s^1 2p^3$) is compensated by the fact that carbon atom can then contract two (2) supplementary bonds whose formation releases more energy (ΔE) [17].

2.2.2. Hybridization of Orbitals

The excited carbon $C^* 1s^2 2s^1 2p^3$ results from the recombination of electrons of $2s$ and $2p$ atomic orbitals. This recombination can be done in three different ways allowing the carbon atom to bind to one or more atoms to form molecules. According to organic chemistry, one of the two $2s$ electrons is promoted to $2p_z$ orbital. So the electronic wave functions for the four weakly bound electrons can mix each

others, thereby changing the occupation of the $2s$ and $2p$ orbitals, since the energy difference between the lower $2s$ and the upper $2p$ levels is low compared to the binding energy in the chemical bonds. This mixing of atomic orbitals is called *hybridization*. In carbon atom, three possible hybridizations occur denoted sp, sp^2 and sp^3.

In the sp hybridization [9, 17, 24], there is linear combination (mixture) of $2s$ orbital and one of the three $2p$ orbitals, $2p_x$ for instance, the other two remaining pure $2p$ orbitals and not involved, ($2p_y$ and $2p_z$ for instance). From these two atomic orbitals, two equivalent sp orbitals are formed, which lie in opposite directions forming between them an angle of 180°, called hybridized orbitals with 1/2 of $2s$ character and 1/2 of $2p$ character. The two pure p orbitals will be normal to each other and normal to the hybrids sp orbitals.

In the sp^2 hybridization [9, 17, 24], three atomic orbitals are involved. The $2s$ and two of $2p$ orbitals, for example $2p_x$ and $2p_y$, are mixed. The three obtained hybridized orbitals are in the same plane, with 1/3 of character $2s$ and 2/3 of character $2p$ and form three σ bonds in molecules. These three hybridized orbitals are oriented so as to make between them angles of 120°. This hybridization leads to triangular molecules (two dimensions). The $2p$ orbital not involved in the hybridization, $2p_z$ remains pure and placed perpendicular to the plane of the three hybrid orbitals. The resulting structure is planar. The hybrid atomic orbitals obtained have large amplitude in the directions of the three nearest neighbor atoms.

sp^3 hybridization [9, 17, 24] is provided by carbon atom through its tetragonal bonding to four nearest neighbour atoms which have the maximum spatial magnitude from each other. In order to make elongated wave functions to these directions, the $2s$ orbital and the three $2p$ orbitals are mixed, forming a sp^3 hybridization. The $2s$ atomic orbital can finally be combined with all three $2p$ atomic orbitals. The four new orbitals are sp^3 hybridized and have 1/4 s character and 3/4 p character. They are oriented along the vertices of a regular tetrahedron (angle of 109° 28'). The resulting arrangement is tetragonal.

These three hybridizations are responsible for allotrope forms of carbon: diamond, graphite, amorphous forms as well as fullerenes and their derivatives, all in an intermediate state of hybridization. The sp^n hybridization is essential for determining the dimensionality of carbon-based structure. Carbon is the only element in the periodic classification that has isomers from 0 dimension (0D) to 3 dimensions (3D). In sp^n hybridization, (n+1) σ bonds per carbon atom are formed; these σ bonds constitute the skeleton for the local structure of n-dimensional allotrope.

2.3. Carbon Allotropes, Including Graphite, Fullerenes and Carbon Nanotubes

The compounds of pure carbon have two traditional allotropes known since thousands of years or centuries. They are: diamond, a hard and colourless solid of carbon atoms sp^3 hybridized, and graphite soft and black solid with sp^2 atoms hybridization. The other pure carbon allotropes of this group are the carbynes and the amorphous carbons. The forms discovered from 1985 to now are carbon nanostructures.

2.3.1. Traditional Forms of Carbon

(i). Diamond

Naturally occurring diamond is almost always found in the crystalline form with a purely cubic structure and orientation of sp^3 bonded carbon atoms as illustrated in reference [9], while synthetic diamond is a randomly mixture of cubic and hexagonal lattices. It is an allotrope being presented in two three-dimensional structures: the face centered cubic (FCC) which is by far the most encountered, and the hexagonal or lonsdaleite [9]. Each conventional cell of FCC diamond contains eight atoms while the primitive cell contains two sites which are (0, 0, 0) and (1/4, 1/4, 1/4).

(ii). Graphite

Graphite corresponds to the stable form of carbon at ordinary temperature and pressure. Its structure is hexagonal with four atoms per unit cell (bulk cell). Its parameters are $a = b = c = 0.2470$ nm and $c = 0.6724$ nm. The carbon atoms arranged in hexagons and strongly linked by covalent bonds form planar layers called graphene sheets or graphene planes. The structure is lamellar and constituted by stacking of graphene planes. This structure confers to the graphite a bi-dimensional modeling [8, 9, 31]. Each atom of the graphene plane is distant from its nearest neighbors of 0.142 nm while the successive graphene planes are separated by 0.336 nm and held together by weak Van der Waals type bonds. Their layering (stacking) is the ABABAB… type, with B plane translated of $a/\sqrt{3}$ with respect to the A plane as shown in Figure 1. There is also a minority form of graphite: the rhombohedral graphite, where the layering (stacking) is rather ABCABC type with c translated of $2a/\sqrt{3}$ with respect to plane A with the distance between the sheets always equal to 0.336 nm. Graphite is a highly anisotropic solid. Structurally, its interplanar spacing (3.35 Å) is quite large compared to the in plane interatomic spacing (1.42 Å). Physically, its stiffness along the plane is quite large because of strong σ bonds and in the perpendicular direction; it is weak because of the Van der Waal's forces. The planes can be cleaved easily making graphite quite a soft material. Also electronically it is anisotropic, because of π and π^* bands overlap. This has metallic conductivity along the plane and semi-conducting perpendicular to the plane. The sp^2 hybridization forms a planar structure. It is made of strong fibers composed of series of stacked parallel layers.

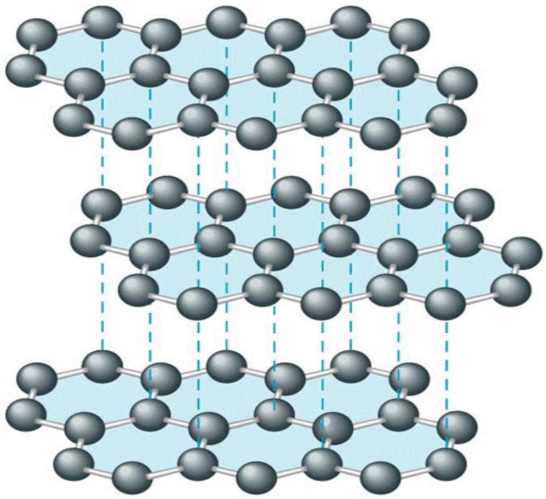

Figure 1. *Hexagonal structure of Graphite in an A-B-A-B layering.*

(iii). Carbynes

They are chains of carbons which have sp bonding [9]. These sp carbon chains can present: a). alternating single and triple bonds; the polyyne, b). only double bonds; the polycumulene. They display some particular chemical properties.

(iv). Amorphous Carbons

The amorphous carbons or free reactive carbons are carbon allotropes that do not have any crystalline structure. They have gain importance in research owing to their rich underlying physics and tremendous applications. The widely known forms of amorphous carbons are: black of carbon, carbon fibers, porous carbon, glassy carbon, diamond like carbon (DLC) and pyrocarbon. Their properties stem from combinations of principally two hybridized forms: sp^2 carbon and sp^3 carbon [9].

2.3.2. New Forms of Carbon or Carbon Nanostructures (CNSs)

(i). Fullerenes

Fullerenes are molecules consisting of sp^2 hybridized carbon sheets, forming a closed sphere structure. These spherical structures are built up out of hexagons and pentagons. The fullerene's formation is based on the introduction of pentagonal, heptagonal or other kind of "defect" rings between the hexagonal rings of the graphene sheets, which favors a higher curvature of the sheet. Each fullerene, by definition, consists of 12 pentagons (Figure 2), since a sphere containing n hexagons cannot be closed otherwise according to Euler's theorem [9].

C_{60} is made of 20 hexagons and 12 pentagons. Each carbon atom is at the intersection of two hexagons and one pentagon. When compared to planar graphene, the introduction of a pentagon gives a positive curvature to the surface. Euler's rules dictate that to create a closed surface, we need a total "curvature charge" of 12 [9]. As a result, all the simple fullerenes will have the same number of pentagons, 12, and differ only by the number of hexagons inserted between them.

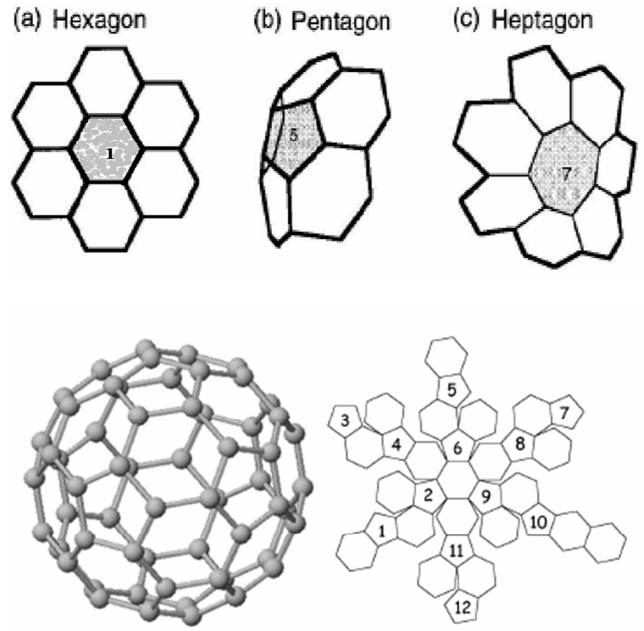

Figure 2. *Left: (a-c) Hexagon, pentagon and heptagon carbon rings in a graphite layer [9]; Right: Fullerene C_{60}, the necessary twelve pentagons to fulfil Euler theorem are numbered.*

Fullerenes possess some unique properties, rendering them suitable for many applications varying from *medicine* to *organic electronics*. Fullerenes have the exceptional capability of being very good *electron acceptors* and *conductor*s, these properties have drawn most attention of scientists. They are nowadays mainly used in *organic solar cells*, *transistors*, and *holographic materials*.

(ii). Carbon Nanofibers

Carbon nanofibers (CNFs) are conical structures that have diameters varying from a few to hundreds of nanometers and lengths ranging from less than a micron to millimeters. The internal structure of carbon nanofibers varies and is comprised of different arrangements of modified graphene sheets. In general, CNFs have a structure which is a mixture of aligned graphene planes as well as a bamboolike or cup-stacked structure, previously ascribed to herringbonelike structure, in other words a nanofiber consists of stacked curved graphite layers that form cones or "cups" [2, 9]. Currently there is no strict classification of nanofiber structures. The main distinguishing characteristic of nanofibers from nanotubes is the stacking of graphene sheets of varying shapes. Defining α as an angle between the fiber axis and the graphene sheet near the sidewall surface, nanofiber *with* $\alpha = 0$ *is a special case in which, one or more graphene layers form cylinders that run the full length of the nanostructure*. This arrangement, with its closed and semi-infinite surface results in extraordinary properties that made this type of nanofiber known to the world as a *carbon nanotube* [8, 28, 9].

(iii). Carbon Nanotubes

Since their discovery [1], countless papers on carbon nanotubes, their properties, and applications have appeared

and generated great interest for future applications based on their *field emission* and *electronic transport properties*, their high *mechanical strength* and *chemical properties* [9]. Carbon nanotubes can be described as cylindrically shaped molecules formed of rolled up single or multilayer sheets of graphitic planes presented on Figure 3. In other words, it can be considered as an infinite strip cut out of a graphene sheet and rolled up along the direction perpendicular to the strip. Geometrically, CNTs have one of the highest aspect ratio of any object in nature. Their length can exceed several millimeters for diameters around ten nanometers. The characteristics of a carbon nanotube, and the position of every atom in it, can be determined by just two integers. All what is needed is the circumference of the tube, which joins the two equivalent atoms along the circumference. These will be superimposed once the strip is rolled up.

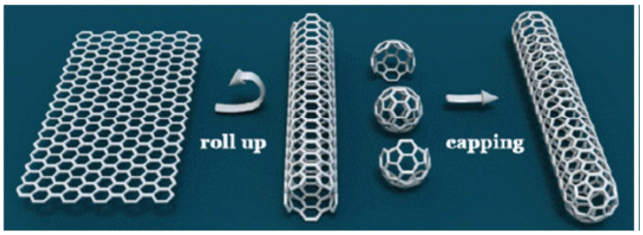

Figure 3. *SWCNT capped with half of a* C_{60} *fullerene molecule.*

The exceptional low-dimensionality and symmetry of carbon nanotubes are at the origin of their spectacular physical properties governed by quantum effects. A carbon nanotube can be of three types: (1) zigzag, (2) armchair and (3) chiral depending on the orientation along which the graphitic planes are folded. When the value of θ (angle between the direction normal to that of the stripe and the folding direction) is, respectively, 0°, 30° or takes any value between, a nanotube is respectively called zigzag, armchair or chiral.

The vector between the two atoms of graphene, $\vec{C}_h$, called the chiral vector is part of the 2 dimensions (2D) crystalline lattice, and denoted by the two integer indices, n and m called Hamada integers [9]. If $\vec{u}$ and $\vec{v}$ are the lattice vectors of a 2D graphene plane as schemed in Figure 4, the chiral or helicity vector is expressed by:

$$\vec{C}_h = n\vec{u} + m\vec{v} \qquad (1)$$

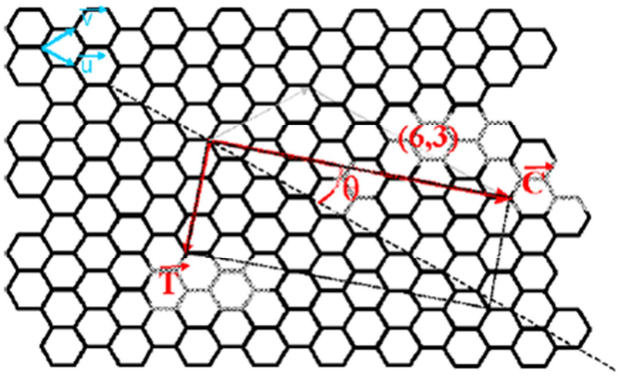

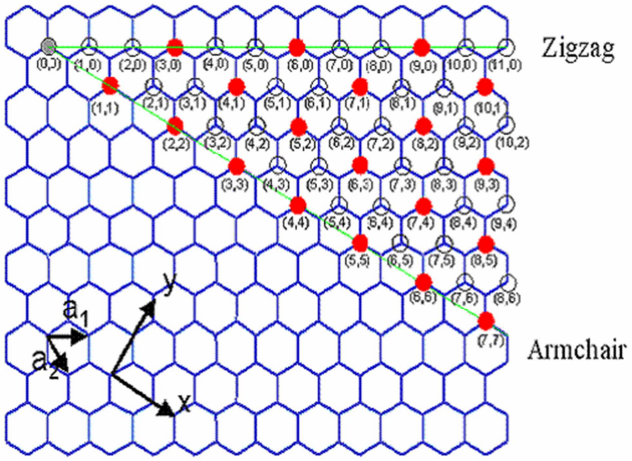

Figure 4. *Left) Graphene layer showing the* $\vec{u}$ *and* $\vec{v}$ *vectors (in blue color); Right) Graphene layer showing the Zigzag and Armchair rolling up conditions [9].*

The simplest termination is a hemispherical cap formed by a half of fullerene. General rules have described the topology of the termination as a function of the Hamada indices (n, m). The prototypical example is shown in Figure 3, but CNTs can also be open ended. According to the integers n and m, CNTs can be metallic, if n-m is a multiple of 3, and semiconductor otherwise.

Two types of CNTs can be distinguished; single walled carbon nanotubes (SWCNTs) or bucky-papers and multi-walled carbon nanotubes (MWCNTs). They can have different properties one another. Typical outer diameters are approximately 1-6 nm for SWCNT and 6-100 nm for MWCNT. MWCNT can be rolled up with their graphene layers concentric or spiral.

(iv). Other Carbon Nanostructures

There are nowadays a plethora of carbon nanostructures. Among them, one can mention the followings [9]. The Single walled carbon nanohorns (SWCNHs): they are typically constituted by tubes of about 2 to 5 nm of diameter and 30 to 50 nm long. They are especially interesting *for hydrogen storage* and *electric field emission*. The Carbon nanosheets (CNSs) are known as *field emission sources* for *high emission*. The Carbon nanoporous are carbon "balls" often linked together as granular *electuary waiver* some holes between which show an amorphous structure. The Carbon nanoparticles (CNPs) are characterized by an average diameter of 80 nanometers. They have in general *catalyst* particles encapsulated in, on the base plane. The Carbon nanobuds (CNBs) are carbon nanostructures in which fullerenes are covalently attached to outer sidewall of CNTs. It is a hybrid material with useful properties, both of fullerenes' and CNTs'. CNBs have been found to be exceptionally good for *field emitter*.

(v). Carbon Nanostructures Defects

A perfect CNS is an abstraction because the hexagonal sp^2 structure can have different types of alterations which can originate from the growth, from the deposit on a substrate, or they can be the result of a chemical treatment. The defects are classified as follows [9].

* Rehybridization Defects

Carbon is not simply sp^2 hybridized in nanostructures, but the hybridization is between sp^2 and sp^3 [23]. Actually, it is $sp^{2+\alpha}$, with $0 \le \alpha \le 1$, due to the curvature of the graphene sheet. There is no curvature with sp^2 pristine [9]. This curvature can produce a local modification of the overlap of the wave functions in comparison to a graphene sheet and cause changes of the density of states (DOS) [9].

* Topological Defects

A typical case of topological defect is the presence of non-hexagonal shaped carbon rings in graphene layer. For example, the presence of pentagon and heptagon pair in the graphene sheet, the so-called Stone-Wales defect or a 5/7 defect [9]. They are localized mainly at tube ends and near tube bending zones. A 5/7 is very much studied for *its implications in the modifications of nanotubes DOS for possible nanodevice applications* [9] and is presented in the Figure 2 (b-c). The *goal is to reach defect engineering*: defect can be used to *interconnect wires* or to *modify DOS to produce nanodevices* at nanometric scale with all implications with regard to the low dimensionality, quantum confinement and *mechanica*l and *transport properties*.

2.4. Conclusion

Carbon is one of the most abundant elements in the earth crust and one of the most fascinating because of the variety of materials it forms and can form. It sometimes appears as a transparent crystal in several forms, with widely different properties. Diamond is composed of sp^3 bonded carbon atoms arranged in tetrahedrons, transparent and one of the hardest materials. In contrast, graphite appears as layered sheets of sp^2 bonded carbon atoms, arranged in a hexagonal network, very soft, semi-metallic and has one of the highest melting points. The discovery of novel carbon-based structures since 1985 [27] has developed a new exciting field of research.

This section has presented the carbon element, its main forms are a consequence of atomic hybridization. More details on carbon nanostructures offer unique physical, mechanical and electronic properties which are promising for a wide range of technological applications.

3. The Dewar-Chatt-Duncanson Model for Characterization of Charge Transfer TM-C in CCVD CNT

It is recalled the DCD model used so far for characterization of charge transfer TM-Carbon in CCVD CNT fullerene cap region, by use of the πσ parameters extracted from HREELS (vibrational spectra) measurements and EELS (Electron Energy Loss Spectroscopy) [23, 5] on CNTs. That charge transfer has been cited in the pass to be responsible of UDOS changes at the vicinity of the Fermi level and influences the absorption transitions [6].

3.1. Bonding and Structure in Alkene Complexes

The Dewar-Chatt-Duncanson model describes the bonding in alkene complexes, which provides with: a σ-type donation from the filled C=C π-orbital and concomitant π-back-donation into an empty π^* orbital on the ethylene. It presents with a synergistic bonding situation: the greater the σ-donation to the metal, the greater the π-back-bonding: as sketched in Figure 8.

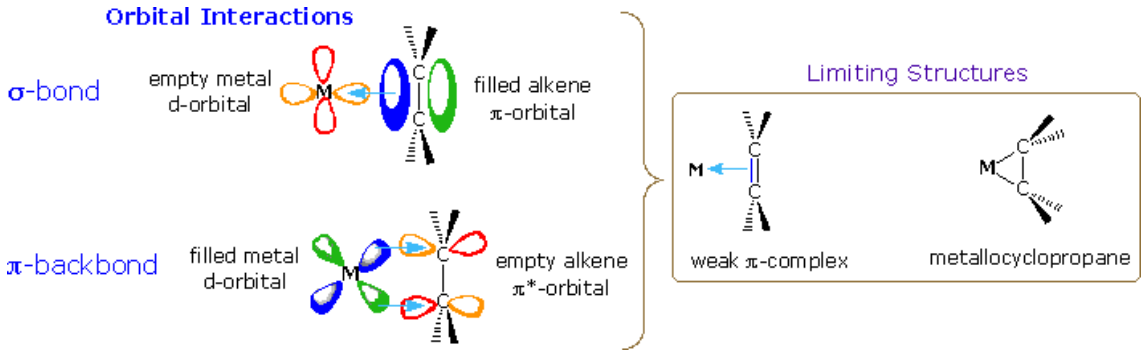

Figure 5. *Alkene-transition metal bonding leading to limiting structures: weak π-complex or metallocyclopropane.*

3.2. The Dewar–Chatt–Duncanson Model

The Dewar–Chatt–Duncanson model is a model in organometallic chemistry which explains the type of chemical bonding between an alkene and a metal forming a π-complex in certain organometallic compounds [19, 20, 32].

The π-acid alkene donates electron density into a metal d-orbital from a π-symmetry bonding orbital between the carbon atoms. The metal donates concomitantly electrons back from (a different) filled d-orbital into the empty π^* anti-bonding orbital of alkene. Both of these effects tend to reduce the carbon-carbon bond order, leading to an elongated C-C distance and a *lowering of its vibrational frequency*. In Zeise's salt $K[PtCl_3(C_2H_4)]\cdot H_2O$ the C-C bond length has increased to 134 picometres from 133 pm for ethylene. In the nickel compound $Ni(C_2H_4)(PPh_3)_2$ the value is 143 pm.

The interaction also causes carbon atoms to "*rehybridise*" from sp^2 to sp^3, which is indicated by the bending of the hydrogen atoms on the ethylene back away from the metal [5, 18]. Some calculations show that 75% of the binding energy is derived from the forward donation and 25% from backdonation [5, 18]. This model is a specific manifestation of

the more general π-backbonding model. The structural distortion of a bound alkene can also be detected by NMR: the J_{CH} of alkene-like sp^2 carbons is typically around 160 Hz whereas sp^3 -like carbons have a J_{CH} around 120 Hz. Unlike carbonyl stretching frequencies, the C=C IR band (around 1500 cm^{-1}) is usually weak and not well-correlated to C-C bond length.

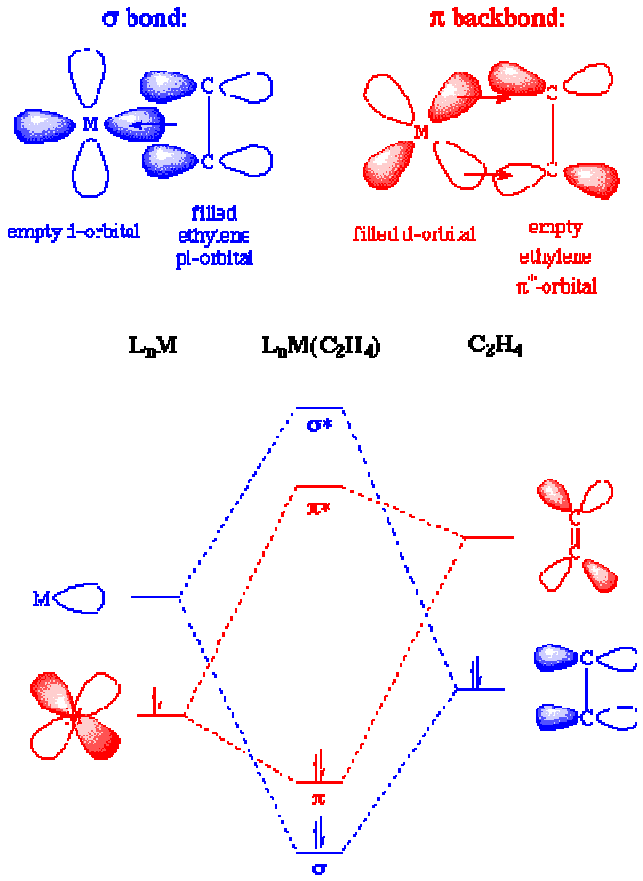

Figure 6. *DCD model showing the different atomic and molecular orbitals involved in the alkene-metal bond and energy diagrams.*

3.3. Binding Modes of Ethylene (alkene) on Dense Faces of Metals

The binding mode of ethylene (alkene) (Figure 8) on clean single crystal metal surfaces to metal atoms [18, 21, 22] may be described by two types of interactions.

A π bonded state where ethylene (alkene) keeps (retains) largely its sp^2 hybridization with conservation of a double carbon-carbon bond has been identified on Cu(111) [18], Pd (110) [18], Ag (110) [18], Ni(100) [18] and Pd(111) [18]. The chemisorption bond of adsorbed ethylene in that case may be explained by the Dewaar-Chatt-Duncanson model [19, 20, 32]. That model describes a synergistic relation in which exists concomitantly a σ-donor interaction [involving a donation (transfer) of charge from the filled π_{2p} orbital of ethylene to empty $d\sigma$ orbital of the metal] denoted σ-donor bonding and a π -acceptor or π -retrodonation [involving a retrodonation (retro-transfer) of charge from $d\pi$ filled orbital of metal to empty antibonding π^*_{2p} of ethylene] (Figure 8).

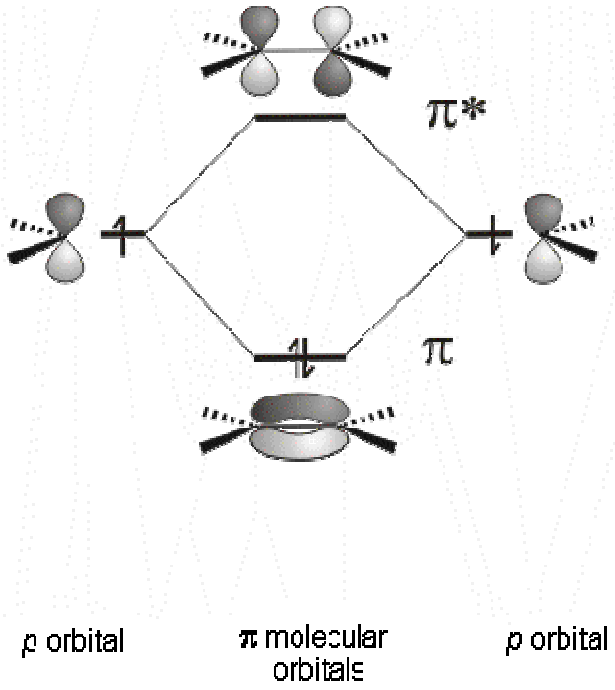

Figure 7. *Energy diagram of ethylene molecule.*

Thus, π -adsorbed ethylene is formally a σ-donor of two electrons, but the π^* molecular orbital allows also ethylene to be a π -acceptor [9, 18]. The relative importance of the two types of interactions (σ donor, π acceptor) depends on the electronic structure of the metal. If the metal possesses a significant positive charge, the σ -donor interaction is favoured. Whereas a more important electronic density on the metal favours a stronger π -acceptor interaction, leading to a more important retrodonation. The retrodonation then lowers the degree of the carbon-carbon bond and increases the hybridization of carbon atoms towards the sp^3 mode. However, in the π complex, the retrodonation plays a relatively minor role, and ethylene keeps (retains) essentially sp^2 hybridization. Adsorption with that type of interaction results in a bonding to the metal substrate, which may be weak (π -complex) or strong (for instance on Pd(111)) [18].

It may also be formed a di-σ bonded state where ethylene carbon atoms are significantly sp^3 rehybridized. When the retrodonation becomes very important, the π -bond in ethylene molecule is almost broken and the π_{2p} orbitals on each carbon atom form covalent (σ) bonds with metal atoms on the surface, leading practically to a simple carbon-carbon bond on the ethylene molecule. Ethylene adsorbed in that state has been observed on Pt(111) [18], Ni(111) [18] and Fe(110) [18].

There exists also other cases where ethylene is adsorbed in an intermediary bonding state with partial rehybridization, sp^{α} $(2 \le \alpha \le 3)$, as on Ni(110) [18], Pd(100) [21, 22], Rh(111) [18], Ru(001) [18] and Fe(111) [18]. This shows that the π

and di-σ bonding modes represent limiting cases, and that the general case corresponds to an intermediate situation. That general case is sketched in Figure 8.

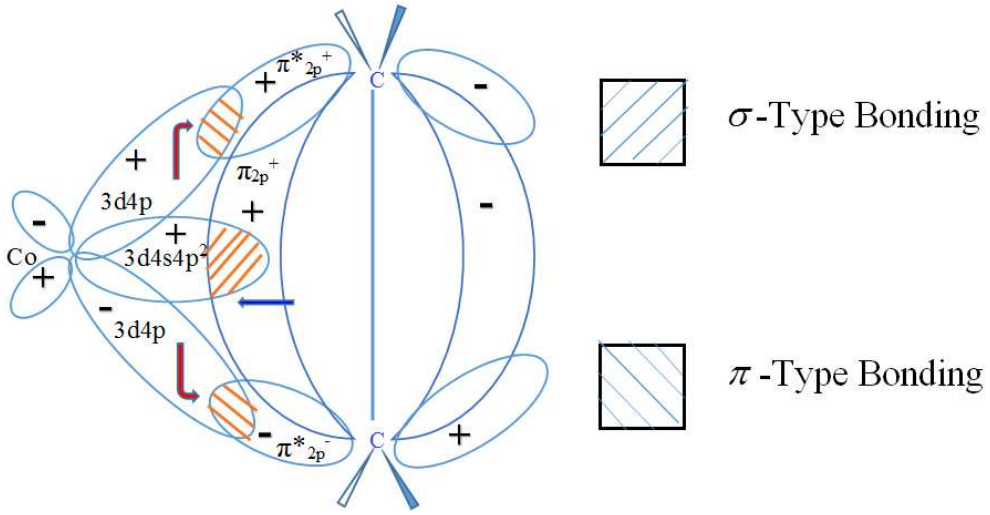

Figure 8. *DCD model for general case of ethylene bonding to transition metal, with variable ethylene carbons hybridization:* $sp^{\alpha}\ (2 \le \alpha \le 3)$.

σ-Donation: $3d4s4p^2\ (\mathrm{d}\sigma)\ [\mathrm{Co}] \leftarrow \pi_{2p}(C_2H_4)$

π-Retrodonation: $3d4p\ (\mathrm{d}\pi)\ [\mathrm{Co}] \rightarrow \pi^*_{2p}(C_2H_4)$

3.4. DCD (Dewar-Chatt-Duncanson) and $\pi\sigma$ Parameters

Two empirical parameters, which use the vibrational spectra of adsorbed C_2H_4 (C_2D_4), have been proposed in order to provide a measure of the degree of rehybridization of ethylene resulting of its adsorption on a metal surface which extends from the sp^2 form to the sp^3 form. The parameterization of vibration frequencies is necessary due to extensive coupling in ethylene between the stretching vibrational mode (symmetrical valence vibration), ν_{CC}, and the in-plane scissoring vibration mode, δ_{CH_2}.

* The $\pi\sigma$ parameter is proposed as a measure of the extent of C_2H_4 rehybridization upon adsorption. That parameter takes into account the vibrational coupling between the $\nu(CC)$ and $\delta(CH_2)$ modes of C_2H_4. The $\pi\sigma$ parameter ranges from zero for gaseous C_2H_4, to 0.38 for Zeise's salt, taken as a model for π-bonded C_2H_4, to unity for $C_2H_4Br_2$ taken as a model for di-σ-bonded C_2H_4. Additionally those metal systems which show high values of $\pi\sigma$ dehydrogenate C_2H_4 whereas those with values less than Zeise's salt bind C_2H_4 weakly and reversibly.

The $\pi\sigma$ [21, 22] parameter combines the *shift towards low frequencies* (wave numbers), of the two coupled modes ν_{CC} and δ_{CH_2} resulting of adsorption, relative to the values in the gas phase. It is defined as:

$$\pi\sigma(C_2H_4) = \left(\frac{1623-\text{band I}}{1623} + \frac{1342-\text{band II}}{1342}\right).\frac{1}{0.366} \qquad (2)$$

where Band I is the higher frequency and Band II is the lower frequency (cm^{-1}), of the coupled pair $\nu_{CC} - \delta_{CH_2}$.

Table 1. *The $\pi\sigma$ parameter of ethylene in gas phase, of Zeise's salt ($K[PtCl_3(C_2H_4)\cdot H_2O$) and of C_2H_4 Adsorbed on Several different Metal Surfaces [21, 22].*

Molecular Species	Ref.	band I, cm^{-1}	band II, cm^{-1}	$\pi\sigma$ Parameter
$C_2H_4Br_2$	Stuv85	1420	1019	1.00
.Pt(111)	Stuv85	1430	1050	0.92
.Fe(111)	Stuv85	1385	1115	0.86
Ru(001)	Stuv85	1400	110	0.85
Ni(100)	Stuv85	1390	1130	0.83
Ni(111)	Stuv85	1440	1100	0.80
Pd(100)	Stuv85	1455	1135	0.78
Fe(110)	Stuv85	1410	1250	0.55
Pd(111)	Stuv85	1502	1229	0.43
Ru(001) + O	Stuv85	1510	1230	0.42
Zeise's Salt	Stuv85	1515	1243	0.38
Pd(100) + O	Stuv85	1340	985	0.30
Pt(111) + O	Stuv85	1370	970	0.27
Cu(100)	Stuv85	1560	1290	0.21
Ag(110) + O	Stuv85	1565	1290	0.14
$[Ag(C_2H_4)]BF_4$	Stuv85	1579	1320	0.12
C_2H_4 gas	Stuv85	1623	1342	0.00

The numbers 1623 and 1342 are respectively the frequencies (cm^{-1}) of ν_{CC} and δ_{CH_2} for C_2H_4 in the gas phase. For the $\pi\sigma$ parameter of C_2D_4, the numbers 1515 and 981 should be respectively used in place of 1623 and 1342. The above parameter is used here in order to characterize the interaction between the tip carbon atoms of CNTs and the catalyst metal particles encapsulated in the cap, since carbon is sp^2 hybridized in graphite sheets, and thus characterize carbon rehybridization and bonding upon catalyst encapsulation.

* The DCD (Dewar-Chatt-Duncanson) parameter [18], not exploited in this work, uses the higher vibration frequency observed between 1100 cm^{-1} and 1500 cm^{-1} in the HREELS of C_2D_4. Each of these parameters is normalized to standard

values; to one for the dibromo-2-2ethylene $C_2D_4Br_2$ (sp^3 hybridization) and zero for the gas C_2H_4 (sp^2 hybridization).

The bonding state formed (obtained) varies with the structure of the metal surface [18] and, other parameters may play an important role (strongly influence) in the (the) formation of the resulting bonding state. The modification of the chemistry of these metallic single crystal surfaces may influence the bonding state of ethylene. Table 1 presents values of $\pi\sigma$ parameter of ethylene in the gas phase, of π-bonded ethylene species obtained on different metal surfaces, of Zeise's salt which is a well-known ethylene-metal complex π-bonded structure [18]. These values are experimentally derived from vibrational frequencies of HREELS spectra of these species [21, 22].

4. Experimental and Results

4.1. Classical DC HF CCVD Mechanism Including Substrate Preparation and the CVD Process

The growth mechanism of CNTs by catalytic CVD process at low temperature on plane SiO_2/Si(100) precovered with catalyst transition metal particles (Fe, Co, Ni), occuring through a three steps process including: (i) an adsorption and decomposition of reactive hydrocarbon species (such as C_2H_2 or a mixture of C_2H_2 and H_2/NH_3) on a reactive top facet of the metallic particle, (ii) a carbon diffusion through the metallic particle under the effect of a concentration gradient between the top and the bottom facets of the metallic particle and finally (iii) an extrusion of closed and cylindrical graphitic shells on side facets of the metallic particles to get closed curved graphitic shells, respectively, is recalled and sketched [31, 33].

4.1.1. Substrate Sample Preparation TM/SiO_2/Si(100)

The substrate sample preparation has already been described elsewhere [31, 33] and is only briefly recalled. The substrates were prepared by SiO_2 deposition of a layer of thickness 5 nm by a DECR (Distributed Electron Cyclotron Resonance) plasma process on a heavily doped Si(100) sample (Sb n-doped with ρ = 3 mΩ.cm; size 8.5×6 ×0.245 mm^3). The choice of a thin SiO_2 film deposition on Si(100) prior to the Co deposition obeys three considerations: (i) avoiding the formation of cobalt silicide, *i.e.* to prevent the Si and Co inter-diffusion; (ii) to coalesce more easily the Co atoms into a narrow distribution of Co islands, due to the larger difference of surface energies between Co and SiO_2 and (iii) a thin enough layer to provide, via electron transport through the oxide layer by tunneling, samples suitable for field emission measurements [31, 33]. This way, SiO_2 is both a non-wetting substrate for metallic particle growth and a protective barrier layer that prevents metal diffusion. The different steps of the substrate treatments and CNT growth are sketched in Figure 9.

The SiO_2/Si(100) sample was then transferred into a stainless steel Ultra High Vacuum (UHV) preparation chamber (base vacuum 10^{-10} mbar) where both Co evaporation and CNTs growth were subsequently performed without air exposure (removal). Co (grade 99.995) was evaporated with an OMICRON EFM3 effusive source at a pressure within 7-10×10^{-10} mbar on the sample heated at 925K ± 20 K during 30 min. The flux rate at 973 K is estimated to 0.025 nm of equivalent layer per minute from an in situ XPS analysis of the Co2p/Si2p signal. In other cases the transition metal is deposited by sputtering within conditions that have been elsewhere described [31].

4.1.2. CNTs Growth by the DC HF CCVD Process on TM/SiO_2/Si(100) Samples

After the substrate preparation and Co deposition, the samples were further transferred to an UHV CVD chamber for the proper growth of the carbon nanostructures (base pressure lower than 10^{-9} mbar). The description of the DC HF CCVD growth of aligned carbon nanotubes has been reported in detail in reference [33]. The gas mixture (100 sccm (standard cubic centimetre per minute) C_2H_2:H_2:NH_3) was thermally-activated by hot filaments (Power P = 150 W), corresponding to a temperature of the filaments of 2100 K, and kinetic energy-activated by polarisation between an anode (Va) and a cathode (Vc) (V_p = Vc-Va = 300 ± 10 V). A first discharge stabilized by the emission of the filaments ensures a high concentration of ionic species as well as activated radicals. A small additional negative extraction voltage applied on the sample (V_e = 10 V) created an extraction discharge, which allowed to withdraw a controlled current density of ionic species (I_e = 2 mA). The temperature (973 K) was controlled and regulated by an independent infrared heater set on the rear side of the sample. A Pt/PtRh thermocouple was contacting the rear side of the sample during the temperature rise. This thermocouple was switched off when the polarisation was started and the contact was then used to monitor the electric current density impinging the sample. The sequences of deposition were the followings: the sample was first heated under vacuum (10 K/min, 573 K, 10 min), then the temperature was risen to 973 K (10 K/min; 40 min) in a H_2 atmosphere at 15 mbar. Acetylene and ammonia were introduced and subsequently the primary discharge and the extraction discharge onto the sample were adjusted to the desired values. The extraction current I_e was set constant. To stop the CNTs growth, successively the acetylene feedthrough, the polarisation, the filaments and finally the hydrogen feedthrough were subsequently switched off. The growth mechanism of CNTs by catalytic CVD process at low temperature, occurs through a three steps process including: (i) an adsorption and decomposition of reactive hydrocarbon species (such as C_2H_2) on a reactive top facet of the metallic particle, (ii) a carbon diffusion through the metallic particle under the effect of a concentration gradient between the top and the bottom facets of the metallic particle and finally (iii) an extrusion of closed and cylindrical graphitic shells on side facets of the metallic particles to get closed curved graphitic shells, respectively. The reactive gas mixture was composed of 20% C_2H_2 in H_2/NH_3 with a variable NH_3 content (0, 1 and 3%). The distance between the substrate and the bottom filaments is 5 mm. The duration of the growth is anyway 15 min. In this way, mutually aligned nanostructures of different densities are obtained, depending on ammonia concentration in the reactive gas mixture. The references as well as the main

characteristics of the sample preparation are displayed in Table 2. According to the nature, the mode of deposition of the catalyst as well as the pressure of the reactive gas mixture, the temperature, the hot filaments power and the plasma power, different carbon nanostructures were allowed to growth, as listed in the following Table 3.

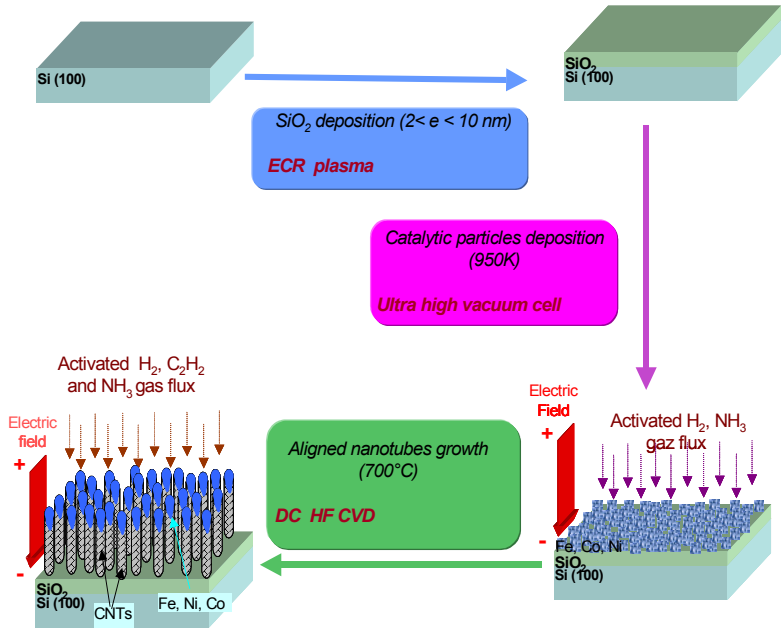

Figure 9. *Sketch of the different steps of substrate preparation and subsequent DC HF CCVD synthesis of CNTs films [34].*

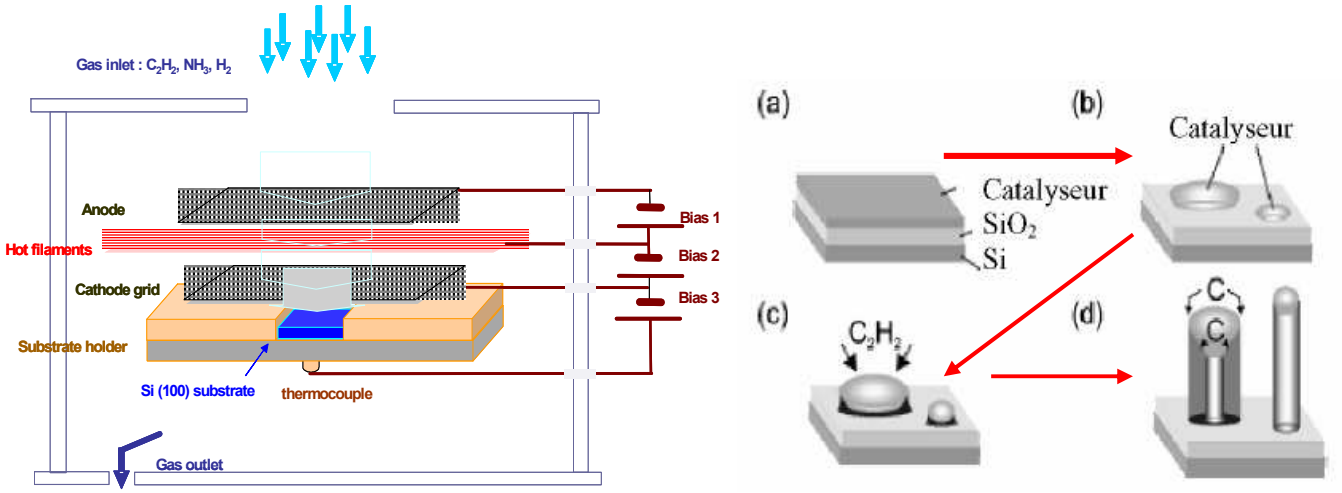

Figure 10. *Left: Scheme of the experimental DC HF CCVD process for CNTs synthesis [34]. Right: Scheme of CNTs growth mechanism in three steps by CCVD at low temperature: a) initial substrate on which was deposited a thin layer of catalyst; b) catalyst sintering into particles; c) decomposition of carbon species; carbon oversaturation of the particle, diffusion of carbon under the effect of the temperature effect and d) graphite precipitation due to successive accumulation [34].*

4.2. CNTs Characterization by Microscopic and Spectroscopic Methods

4.2.1. Surface Analysis, Structural and Morphological Characterizations by SEM (Scanning Electron Microscopy) and TEM (Transmission Electron Microscopy)

One proceeds to the morphological and structural characterizations through surface analyses by SEM and TEM, aiming to obtain a qualitative and overall view of the characteristics of CNTs samples. TEM observations were performed on a TOPCON 002B microscope operating at 200 kV. The sample is scratched with a diamond tip and the material is directly pulled onto a carbon membrane which is drilled with holes in order to get more accurate observations. SEM observations were performed on an XL30S-FEG PHILIPPS working at 3 KV. The nature of the carbon deposit was also probed by Raman spectroscopy and XPS.

4.2.2. Surface Analysis by Raman Spectroscopy (RS)

The Raman spectra (RS) (or HREELS spectra) of five samples were recorded on a Renishaw spectrometer using a He-Ne laser light source at $\lambda = 628.8\,nm$, $(h\nu = 1.9615\,eV)$ equipped with a Notch filter and working in the backscattering geometry. They were in a first time destined to

probe the nature of the carbon deposits. The samples include films of: a CNTs sample grown by PE HF CCVD (Figure 11), carbon nanoparticles (CNPs), carbons nanotubes (CNTs), carbon nanofibers (CNFs) parallel to the substrate and carbon nanofibers (CNFs) normal to the substrate (Figure 12 and Figure 13). We expected the HREELS experiments on the samples under study allow to retrieve their $\pi\sigma$ parameter values and to characterize the eventual carbon↔metal charge transfer through rehybridization.

Table 2. *Main preparation characteristics of carbon nanostructures grown on SiO_2 (5 nm)/Si(100) samples. Other conditions are: C_2H_2:H_2: 20:80; distance filaments-substrate: 5 mm; gas flow: 100 sccm.*

Sample	Catalyst	TM deposition Process S: sputtering E: evaporation	TM/Si	P_f (W)	P_e (mW)	Pressure (mbars)	T (K)	Nanostructure
I Nanot 24	Co	S		150	10	15	973	CNFs with graphene // substrate
II Nanot 29	Co	S		150	30	15	973	CNTs (poorly oriented)
III Nanot 30	Co	E	0.33	150	30	15	973	CNFs with graphene ⊥ substrate
IV Nanot 31	Co	E	0.87	150	30	15	973	CNTs
V Nanot 36	Co	E		100	20	15	973	CNPs
VI Nanot 42	Co	E		145	20	15	1083	CNTs (highly oriented)
VII FLN1	Co	E		140	20	15	973	CNTs (medium oriented)
VIII FLN2	Co-Fe	E		140	20	15	973	CNTs (highly oriented)
IX FLN4	Co	E		140	20	5	973	CNWs

Table 3. *Main characteristics of the carbon nanostructures grown: CNTs, CNFs, CNPs and CNWs are carbon nanotubes, nanofibers, nanoparticles and nanowalls, respectively.*

Samples	Nanostructure	Outer diameter (nm)	Inner diameter (nm)	Length (nm)	Density (μm^{-2})
I	CNFs with graphene // substrate	25	0	110/	472
II	CNTs (poorly oriented)				
III	CNFs with graphene ⊥ substrate	20	0	140/	494
IV	CNTs	30	9	375/	400
V	CNPs				
VI	CNTs (highly oriented)	25	5	400/	349
VII	CNTs (small oriented)			< 100	
VIII	CNTs (highly oriented)	10	4	187/	1000
IX	CNWs				

4.3. Results

4.3.1. Morphological and Structural Investigations by SEM and TEM

Figure 11 shows the SEM (a) as well as the HRTEM (b) images of aligned DC HF CCVD long carbon nanotubes or carbon nanofibers vertically oriented relative to the substrate surface. The catalyst metal is made of cobalt nanoparticles. Moreover the tubes are of the bamboo-shape type with always a metallic particle on top of the tubes. These metallic particles exhibit an anisotropic shape (oblong) rather than the isotropic shape observed in the other CCVD processes. In addition, the high resolution shows some defects within the graphitic shells. The lateral size is around 15–20 nm with a narrow size distribution. This size distribution is quite similar to the initial Co catalytic nanoparticles one. Catalyst particles fragments are smeared in the internal side wall shells of the tubes.

As the SEM and TEM images clearly illustrate in Figure 12 and Figure 13, respectively, the carbon nanostructures prepared in this study display widely different morphologies according to some variable parameters of the catalyst preparation (amount of cartalyst deposited measured by the surface ratio Co/Si, mode of Co deposition, and growth conditions (temperature, plasma power and hot filaments power, pressure) reported in Table 2. Under conditions where the catalyst is deposited by UHV atomic evaporation at moderate pressure (5-15 mbar), it is possible to control the nature of the carbon nanostructures [31]. Carbon nanowalls (CNWs) are prepared at low pressure (5 mbar) (Figure 12-F). These are graphene sheets that merge in the direction normal to the surface (Figure 13-F), when the energy of the ions impinging the surface is rather high. Carbon nanoparticules (CNPs) are prepared when the power of the hot filaments is low (Figures 12-C and 13-C). Carbon nanofibers were prepared under different conditions. When the plasma power is high and the catalyst surface concentration is low, then graphene sheets grow in a direction normal to the surface (Figures 12-B and 13-B), forming conical nanostructures with the metal particle on top of it. When the catalyst is prepared by sputtering and the plasma power is rather low, then CNFs can grow with graphene sheets parallel to the surface (Figures 12-A and 13-A). Strong adhesion of the catalyst to the substrate and low energy ions can explain this mode of growth. Within medium plasma power, carbon nanotubes can yet be grown with graphitic planes in a parallel direction to the fiber axis can yet be prepared (Figure 13-D). These samples however display different mutual orientation. Highly oriented films are obtained under optimized conditions (Figure 12-D). Poorly oriented films are also obtained (Figure 12-E) and the nanotubes show more defects (Figure 13-E). Anyway the presence of hot filaments heated around 2200 K must be stressed. They provide hydrogen radicals that are very reactive towards all kinds of amorphous carbon. This is checked in Raman spectra (Figure 14). The most intense Raman spectrum corresponds to sample V as the etching of carbon by hydrogen radicals is less effective. Thus probably carbon not only surrounds the particle but also is spread onto the surface of the sample. It is beyond the scope of this section to discuss the

Raman spectra of these different carbon nanostructures. We must just underline that whatever the sample the D band due to disordered carbon and the G band due to the main tangential vibrations in graphene sheets or shells are very narrow. This indicates that the carbon deposit is selective.

4.3.2. Vibrational Spectra to Ascertain Charge Transfer TM-C through πσ Parameter Values: Results

The Raman spectrum (Figure 11 (c)) exhibits very sharp D and G bands with many narrow substructures within these band domains. The sharp and narrow (FWHM=13 cm^{-1}) G band at 1591 cm^{-1} has two weak substructures on each side at 1555 cm^{-1} and 1606 cm^{-1}, respectively, *quite characteristic of the occurrence of CNTs* [32]. The small FWHM of band G and the weak D band are both qualitative indications of the absence of any other carbon deposit as well as the absence of many defects within the nanotubes. It may be observed that the G and D bands are concomitantly shifted towards lower wave numbers compared to their positions for ethylene in the gas phase, taking then the values 1623 cm^{-1} and 1342 cm^{-1} respectively. Thus, with a D band located at 1310 cm^{-1}, one derives a $\pi\sigma$ parameter with average value $\pi\sigma = 0.12$ which is equal to that of the system $[Ag(C_2H_4)]BF_4$ and near that of the $Ag(110) + O$ system which is 0.14 (Table 1).

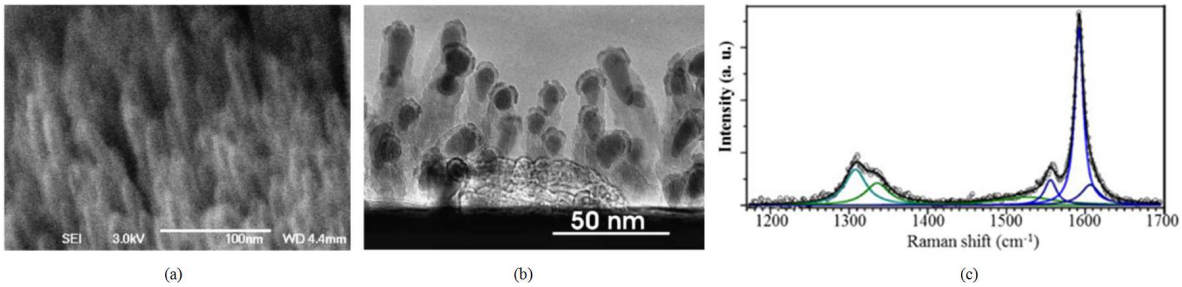

Figure 11. *SEM (a) and HRTEM (b) images and Raman spectrum (c) of aligned DC HF CCVD long carbon nanotubes or carbon nanofibers vertically oriented relative to the substrate surface. The synthesis process was catalysed by cobalt nanoparticles.*

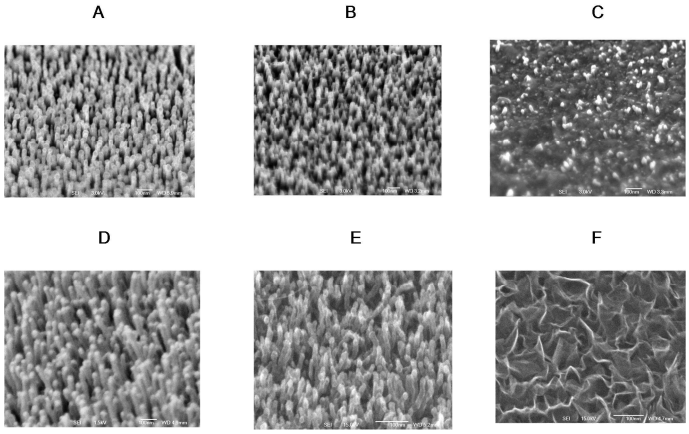

Figure 12. *SEM images of carbon nanostructures. A: sample I (CNFs with graphene // substrate); B: sample III (CNFs with graphene ⊥ substrate); C: sample V (CNPs); D: sample IV (CNTs Medium Oriented); E: sample VIII (CNTs Highly Oriented); F: sample IX (CNWs).*

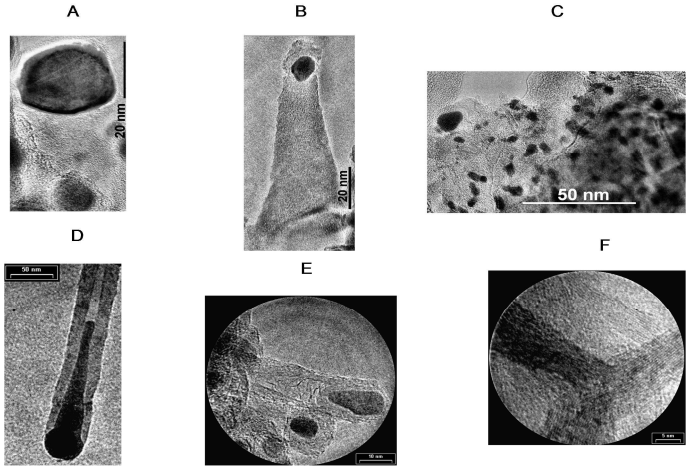

Figure 13. *TEM images of carbon nanostructures. A: sample I (CNFs with graphene // substrate); B: sample III (CNFs with graphene ⊥ substrate); C: sample V (CNPs); D: sample IV (CNTs Medium Oriented); E: sample VIII (CNTs Highly Oriented); F: sample IX (CNWs).*

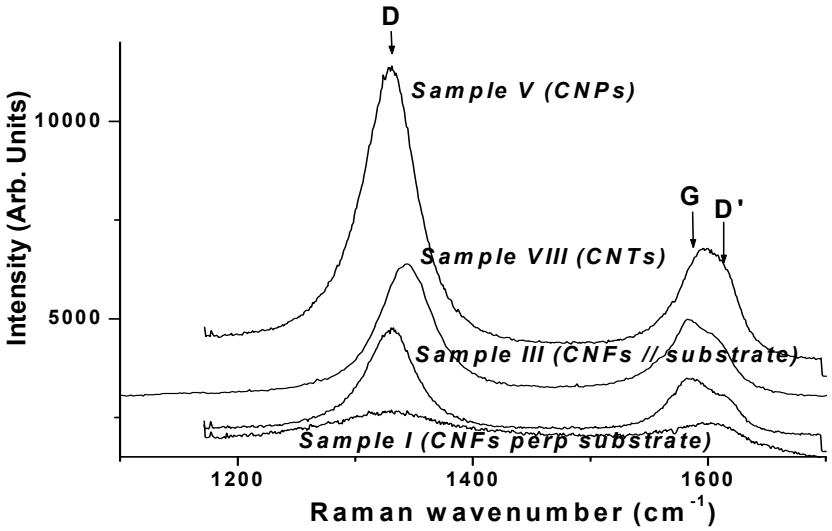

Figure 14. *Raman spectra of carbon nanostructures [8].*

The capacity of the $\pi\sigma$ parameter to measure C_2H_4 rehybridization does not depend on the details of the structure of the C_2H_4-metal complex. For π-bonded C_2H_4 ($\pi\sigma \leq 0.4$) the degree of rehybridization is small precisely because C_2H_4 interacts only weakly with the substrate via the π-electrons, regardless of the bond lengths. For strongly interacting C_2H_4 ($\pi\sigma \geq 0.4$) vibrational coupling between the external C_2H_4-metal vibrations (phonons) and the internal $\nu(CC)$ and $\delta(CH_2)$ modes should also be small since the external modes are generally less than 500 cm^{-1} and far removed from the 1000 -1450 cm^{-1} range of the internal modes. In any case, it is important to remember that C_2H_4 rehybridization is reflective of the state of bonding of C_2H_4, and the $\pi\sigma$ parameter therefore is a *measure* of the bonding of adsorbed ethylene.

We found $\pi\sigma = 0.12$, located in the range of π-bonded carbon in the C-Metal complex. Though that system remains a π complex one, there does exist a substantial interaction C-M, thus a charge transfer from carbon to the metal through π-electrons of graphite matrix (corresponding to the forward σ-donation). Reversely, through retrodonation from metal to carbon (or π-backdonation), charge is transferred back to tip carbons in the graphene matrix. The later in case the retrodonation becomes more important may enhance the DOS of unfilled states of tip carbons around the Fermi level. That hypothesis is in agreement with Chiou et al. [6] and may support the conclusions derived from reference [17]. Moreover, fullerenes are known to be *good electron acceptors and conductors* [9]. They also have a great electronic affinity. It is recalled that the RS spectra of carbon nanotubes of Figure 14 exhibit the same trends that those observed for the exhaustively analyzed sample of Figure 11 (c). Thus, on the *Sample III (CNFs // substrate)*, the main G and D bands are respectively located around 1586 cm^{-1} and 1326 cm^{-1}, leading to $\pi\sigma = 0.10 \pm 0.01$. On the *Sample VIII (CNTs)*, the same bands are observed around 1590 cm^{-1} and 1335 cm^{-1}, yielding $\pi\sigma = 0.08 \pm 0.01$. And for the Sample V (CNPs), the bands are located around 1605 cm^{-1} and 1310 cm^{-1}, respectively; yielding $\pi\sigma = 0.10 \pm 0.01$. All these values of $\pi\sigma$ are within the range of sp^2 hybridization of carbon atoms. These results point to CNTs in what we entitled bonding STATE1.

5. Discussion of These Results

5.1. Electronic Structure of the Carbon Nanotube Tips

For emitters such as CNTs, most electrons are emitted from the tips. Spatially resolved electron energy loss spectroscopy showed that the local electronic structure at the tip could dominantly determine electron emission from a CNT [6]. Since tips have a smaller radius of curvature, the local electronic structures at tips were proposed to be different from those of sidewalls [6]. Theoretical investigations showed that the ends of the tube should have different electronic structures due to the presence of topological defects or localized states [6, 9]. Carbon *K*-edge electron energy-loss spectroscopy [23] and X-ray absorption near-edge structure (XANES) [8] measurements for CNTs suggested that the overall features of the electronic states of carbon atoms in the nanotubes are very similar to those of graphite. On the other hand, photoemission measurements found that at the tip, the C 1*s* core level could shift to a higher binding energy and the density of states (DOS) both sides of the Fermi level, E_F, was enhanced [35]. More recently, scanning photoelectron microscopy (SPEM) measurements for the aligned CNTs also revealed that the tip has a larger DOS near E_F than the sidewall [36].

Angle-dependent XANES and scanning photoelectron microscopy (SPEM) measurements have been performed to differentiate local electronic structures of the tips and sidewalls of highly aligned carbon nanotubes [6]. The intensities of both π^* - and σ^* -band C *K*-edge XANES features were found to be significantly enhanced at the tip, when the incidence angle θ between the surface normal and the incident synchrotron radiation decreases from grazing incidence (θ near 90°) to normal incidence (θ near 0°). SPEM results also show that the tips have a larger density of states (DOS) and a higher C 1*s* binding energy than those of sidewalls. The increase of the tip XANES and SPEM

intensities is quite uniform over an energy range wider than 10 eV in contrast to earlier finding that the enhancement is only near the Fermi level [36]. Since the intensity is approximately proportional to the density of the unoccupied C 2*p*-derived states, the results indicate an increase of the absorption intensity with the decrease of θ not only for the unoccupied π^* states but also for the σ^* states. Thus, C *K*-edge XANES result shows that the DOSs of both unoccupied π^* and σ^* bands are enhanced at the tip. SPEM shows that the tips have a larger valence-band DOS over the whole energy range plotted both sides of the Fermi level. The tips have a higher C 1*s* core-level intensity. The C 1*s* spectrum of the tip apparently shifts toward a higher binding energy by about 0.2 eV relative to those of the sidewall spectra. The difference intensities between the tip and sidewalls are found to slowly and smoothly vary over an energy range larger than 10 eV, from -10 eV below E_F (or the valence band maximum) to +10 eV above E_F (or conduction band minimum). These difference intensities do not show prominent features near E_F. This suggests that *defect and dangling-bond states are not the only origins of the enhancement of DOS at the tip*, because defect and dangling-bond states should be near E_F and not spread over such a large energy range.

5.2. Physical Origins of the Increase of DOS at the Vicinity and Both Sides of the Fermi Level

Sharp XANES resonance or dangling-bond states due to topological defects near the ends of the capped CNTs were proposed previously for the cause of the increase of DOS at the tips [6, 9]. It was suggested that unpaired π bonds could occur in bent vertical graphite sheets, which could yield localized states in the gap orientated in the direction of the field and might have the optimal stable electronic configuration for field emission [6]. But since from SPEM, the difference intensities between the tip and sidewalls are found to slowly and smoothly vary over an energy range larger than 10 eV, from -10 eV below E_F (or the valence band maximum) to +10 eV above E_F (or conduction band minimum) and, these difference intensities do not show prominent features near E_F, it was suggested that defect and dangling-bond states were not the only origins of the enhancement of DOS at the tip, because defect and dangling-bond states should be near E_F and not spread over such a large energy range. Thus, the concern is now the physical origins that cause the increase of DOS at the tips apart from topological defects and dangling bonds, and the understanding of the mechanisms of electron field emission and charge transfer at the tips.

CHARGE TRANSFER TRANSITION METAL-CARBON

One may consider Charge transfer within an organometallic complex and rehybridization of sp^2 carbon upon adsorption on a metallic surface. The bonding is then described within the DCD model (Section 3). The charge transfer proceeds through a synergetic forward donation from π_{2p} electrons of carbon to unfilled $3d4s4p^2$ $(d\sigma)$ $[Co]$ states denoted $\sigma-\text{Donation}$, and a concomitant retrodonation from $3d4p$ $(d\pi)[Co]$ filled orbitals of metal to π^*_{2p} unfilled orbitals of carbon, denoted $\pi-\text{retrodonation}$. Considering the electronic contrast between cobalt and carbon atoms, the retrodonation should dominate and justify part of the increase of the density of state (DOS) at the tips. The values of the $\pi\sigma$ parameter retrieved from the studied aligned carbon nanotubes films may support the later suggestion. Of course, the presence of topological defects and dangling bonds implies sp^3 hybridization of a certain amount of carbon atoms. Their influence should be depicted at the Fermi level. More, apart from defects and dangling bonds, initial carbon atoms may be rehybridized through their interaction with the metal particles. A measure of that rehybridization upon adsorption constitutes a measure of the bonding state and that of charge transfer to the graphene matrix, thus explaining the DOS increase at tips. In fact, the values of $\pi\sigma$ obtained are within the domain of π-complex systems ($\pi\sigma \leq 0.4$), ascertaining a rather weak interaction carbon-metal. It doesn't mean that there is zero rehybridization; the difficulty resides in its measure. These values of $\pi\sigma$ may also be consistently correlated with the geometrical approach developed in reference [17].

BOND HYBRIDIZATION IN MIXED sp^2/sp^3 BONDED MATERIALS

An attempt has been made for determining bond hybridization in mixed sp^2/sp^3 bonded materials while combining NEXAFS and Raman spectroscopies [13]. NEXAFS measurements were performed on a variety of carbon materials, covering a range of hybrid bonding character from pure sp^3 type to pure sp^2 type: diamond, chemical vapour deposited (CVD) diamond films of varying quality, diamond-like carbon (DLC) films, and graphite were examined with this NEXAFS and these measurements were compared with Raman spectroscopy results and scanning electron microscopy images for carbon film morphology. For the mixed $sp^2$and sp3 bonded DLC materials, NEXAFS does not suffer from the large Raman cross-section difference between sp^2 and sp^3 type bonds, thus allowing unambiguous characterization of carbon thin films with a broader range of sp^2/sp^3 bonding ratios than possible with Raman spectroscopy alone. This capability was used to *qualitatively* determine the transition point where the sequential-CVD carbon film growth technique produces predominately sp^3 or sp^2 bonded material.

The primary tool that has arisen in the literature to distinguish between the sp^2 (graphitic) allotrope and the sp^3 (diamond) allotrope has been Raman spectroscopy. This technique uses a laser to probe the density of optical photon states in the bulk material, yielding an indirect measurement of the predominant chemical bonding in a mixed hybrid material. This technique suffers from several drawbacks, one of which is the large difference in the Raman cross section for the two allotropes of carbon [13]. The Raman cross section for graphitic features can be up to 50 times that of diamond [13]. This leads to a dramatic sensitivity to sp^2 bonding in a mixed hybrid material. A second shortcoming of the Raman measurement is the dependence on the long range order parameter of the material. The Raman incident photon wavelength is on the order of microns, which leads to strong crystal size dependence and a critical crystallite size. These limitations weaken the utility of Raman spectroscopy for studying ‘‘diamondlike carbon’’ (DLC) and amorphous or nanocrystalline carbon. To overcome these problems, the

near-edge X-ray absorption fine structure (NEXAFS) technique had been applied.

In that study, standards of natural diamond and highly ordered pyrolytic graphite (HOPG) were measured using carbon 1*s* (NEXAFS), scanning electron microscopy (SEM) and Raman spectroscopy, along with a series of carbon films deposited *sequentially* on silicon. The carbon films were prepared in a "sequential-(CVD)" deposition system [13]. In this system, one can independently vary the fluxes of atomic species arriving at the substrate, via separate atomic sources which impinge on a rotating sample platten. The films were grown at controlled conditions of 10 Torr total pressure in an ambient of mainly helium, which was used as a separator gas in this reactor. The growth conditions include a substrate temperature of 850 °C, a growth time of 10 h hydrogen flow rate of 200 sccm, carbon flux of 200 sccm helium in a carbon sputtering cell, and a sample platten rotation rate of 200 rpm. For this carbon film series, the flux of monoatomic hydrogen to the surface was varied via the amount of current applied to a dissociation filament in the hydrogen source. All the other deposition variables were held constant. The samples were then measured *ex situ* with SEM, NEXAFS and Raman spectroscopy.

In the carbon film deposition series the power to the hydrogen cracking filament was varied from 750 to 350 W with all other deposition conditions held constant. NEXAFS and Raman lineshape analysis results allow unambiguous distinction of bonding type, starting from pure sp^3 type (diamond, H 750 W) to pure sp^2 (graphite, H 350 W), *evidencing qualitatively* a *transition point* where the sequential-CVD carbon film growth technique produces predominately sp^3 or sp^2 bonded material for (H 350 W). This determination method is qualitative and depends on the films growth process. A systematic calibration method allowing to implement the determination of the ratio of sp^2/sp^3 bonds is not settled yet. Moreover, the carbon nanotube after its synthesis is a "frozen" system. No parameter is expected to vary.

Conclusions

This part of the article (including sections 4 and 5) addresses important aspects of XAS signal recorded from CNTs grown in a main direction normal to a flat substrate by classical DC HF CCVD. It also describes that growth method in details. Such CNTs are aligned almost vertically on the substrate and are useful for field emission purposes. The article [5] aims to tackle characterizing the nature of charge transfer between TM catalyst and carbon atoms at the level of the tips, thus allowing to discriminate between sp^2 and sp^3 hybridized carbon atoms, using the $\pi\sigma$ parameters retrieved from the so called Dewar-Chatt-Duncanson model [18, 19, 20, 21, 22] and complementary vibrational spectra data on these CNTs [13, 23]. The presence of non-hexagonal shaped carbon rings consists in topological defects which are localized mainly at tube ends and near tube bending zones. The contamination and rehybridization of the CNTs are intrinsically related to the curvature of their graphene layers.

A literature survey on carbon, carbon graphite, fullerenes and carbon nanotubes is presented in Section 2 and describes their main forms, characteristics and properties (physical, mechanical and electronic). Among them are mentioned hybridization, carbon allotropes including traditional forms of carbon and new forms of carbon among which fullerenes, carbon nanofibers and carbon nanotubes and inherent defects.

In Section 3 is theoretically attempted the characterization of charge transfer TM-Carbon at the fullerene cap region within the Dewar-Chatt-Duncanson model, by use of the $\pi\sigma$ parameters extracted from vibrational spectra measurements [13, 21, 22, 23] on CNTs. It covers the bonding and structure in Alkene-Transition Metal Complexes, the Dewar-Chatt-Duncanson model [19, 20, 21, 22, 37], the binding modes of ethylene (alkene) on dense faces of metals, the $\pi\sigma$ parameters retrieved from the DCD model.

Section 4 is the recall of the experimental one including PE HF CCVD synthesis of studied CNTs and Raman spectroscopy experiments as well as vibrational spectra results and SEM and TEM characterization of the same samples. The experimental vibrational spectra of CNTs and CNFs allow ascertain charge transfer TM-C through the $\pi\sigma$ parameter values.

Section 5 is devoted to a discussion of results: electronic structure of the carbon nanotube tips by XANES and SPEM, physical origins of the increase of DOS at the vicinity and both sides of the Fermi level including: defects (XAS and SPEM), curvature induced rehybridization of carbon atoms at the fullerene cap, charge transfer TM-C (vibrational spectra measurements, DCD model and $\pi\sigma$ parameters) and bond hybridization in mixed sp^2/sp^3 bonded materials. From previous Angle-dependent XANES and scanning photoelectron microscopy (SPEM) measurements, the intensities of both π^*- and σ^*-band C *K*-edge XANES features were found to be significantly enhanced at the tip, when the incidence angle θ between the surface normal and the incident synchrotron radiation decreases from grazing incidence (θ near 90°) to normal incidence (θ near 0°). SPEM results also show that the tips have a larger density of states (DOS) and a higher C 1*s* binding energy than those of sidewalls. The difference intensities between the tip and sidewalls are found to slowly and smoothly vary over an energy range larger than 10 eV, from -10 eV below E_F (or the valence band maximum) to +10 eV above E_F (or conduction band minimum), showing no prominent features near E_F thus suggesting that defect and dangling-bond states are not the only origins of the enhancement of DOS at the tip, since defect and dangling-bond states should be near E_F and not spread over such a large energy range. The $\pi\sigma$ parameter values retrieved from vibrational spectra measurements through the DCD model are within the range of sp^2 hybridization of carbon atoms ($\pi\sigma \leq 0.4$). Meanwhile, through retrodonation from metal to carbon (or π-backdonation), charge is transferred back to tip carbons in the graphene matrix. The later in case the retrodonation becomes more important than forward donation (σ-donation) may enhance the DOS of unfilled states of tip carbons around the Fermi level. Bond hybridization in mixed sp^2/sp^3 bonded materials is addressed, but cannot be implemented for a "frozen" system as CNTs. The above hypothesises and conclusions are not in contradiction with the conclusions derived from the geometrical approach developed in the reference [17].

Finally, by mastering the majority direction of this charge transfer TM-C, thus mastering the capability to willingly orientate this charge transfer direction, it was concluded this work may have some implications in the defect engineering through the judicious choice of the TM catalyst to be used for the PE HF CCVD synthesis of the carbon nanotubes [5, 9, 24]. Indeed, defect can be used to *interconnect wires* or to *modify the DOS to produce nanodevices*. This way, in the next section 6, we propose a promoted catalyst of DC HF CCVD allowing to lower the charge transfer TM-C at the tip region of the CNT and all along the CNT side wall shells.

6. The Effect of K and Cs Atoms on Ethylene Adsorption on the Pt(111) Surface

6.1. Conversion of Adsorption Mode Induced by Alkali Precoverage

The adsorption of C_2H_4, on bare and Cs-, K-precovered Pt(111) surfaces has been investigated in the past, using UPS and TDS [38]. Both coadsorbates (K, Cs) induce the appearance of more loosely (π-bonded) adsorbed species. In the presence of alkali adatoms, these new species are almost undistorted compared to gaseous, multilayered ethylene and ethylene adsorbed as a monolayer at 37 K. The C_2H_4 valence-level shifts observed in the presence of K (Cs) are consistent with the electrostatic field existing in the vicinity of the alkali metal adatoms [39].

Introduction

The adsorption and reactions of ethylene (and acetylene) on the dense faces of several metals and particularly on Pt(111) [38, 39, 40, 41, 42, 43-63] have been thoroughly investigated by various means including low energy electron diffraction (LEED) [43, 44], ultraviolet photoelectron spectroscopy (UPS) [41, 42, 45, 50] and X-ray (XPS) spectroscopies [45, 50], high resolution electron energy loss spectroscopy (HREELS) [47, 48], thermal desorption spectroscopy (TDS) [41, 42, 48, 49, 52, 53, 56, 58, 61], Auger electron spectroscopy (AES) [46], infrared adsorption spectroscopy (IRAS) [60, 62], secondary ion mass spectroscopy (SIMS) [52, 61] and X-ray absorption near-edge spectroscopy (XANES) [40, 42, 52, 63]. After adsorption at 100 K, the main reaction path is partial desorption and conversion with temperature of a di-σ-bonded species into ethylidyne, acetylide and/or methylidyne, disordered carbon and graphite. In reference, [64], it was shown using UPS (ultraviolet photoelectron spectroscopy) that below 52 K, a π-bonded species (where the C=C double bond is preserved) exists prior to the formation of the multilayer. The existence of other forms of adsorbed ethylene (π-bonded species) has been proved on O-precovered Pt(111) [48] and on O-precovered Ru(0001) [65], on K-precovered Pt(111) [61, 66, 67], and on Cs-precovered Pt(111) [64]. In all these cases, π-ethylene desorbs at lower temperatures than di-σ-ethylene which also converts into ethylidene and ethylidyne at low coverages of the coadsorbate.

We recall here the discussion of UPS and TDS results obtained on bare and K-, Cs-precovered Pt(111) surfaces [38]. They are explained by the formation of π-bonded species (in the presence of the surface precovered by alkali atoms). Strong valence-level binding-energy shifts are observed in the presence of alkali adatoms. Such a behavior is also discussed.

3. Results

The temperature range in which molecular ethylene desorbs gives an idea of the desorption energy [68] which is expected to be higher for di-σ-ethylene (where covalent bonds exist between the metal and the carbon atoms [67]) compared to π-bonded molecules (σ-donation and π-back-donation [69]) or physisorbed molecules. After calibration, the amount of desorbed hydrogen leads also to the composition of the CH_x. residue with temperature. Such a method has been used successfully in the pass, in conjunction with HREELS for instance, to follow the transformation of ethylene into ethylidyne and its further decomposition [48].

TDS experiments

TDS data have been obtained for various initial coverages of alkali metals [64, 67]. At 95 K, ethylene adsorbs on the bare surface as a di-σ species. The conversion of di-σ ethylene into π-bonded ethylene appears progressively with the alkali coverage and is complete at about 0.17 ML. It goes along with the disappearance of ethylidyne.

Figure 15 shows the desorption spectra of ethylene adsorbed at 95 K onto clean Pt(111) (Figure 15a), Pt(111) precovered with Cs (Figure 15b -0.205 ML) and with atomic oxygen (Figure 15c - about 0.25 ML). The heating rate was 10 K/s. The collected spectra are in good concordance (agreement) with previous results [48, 64, 67]. The presence of coadsorbed alkali metal atoms or oxygen atoms leads to the appearance of desorption states at lower temperatures than the desorption temperature of the di-σ species (260-280 K). In the presence of alkali atoms, ethylene desorbs at about 130-150 K.

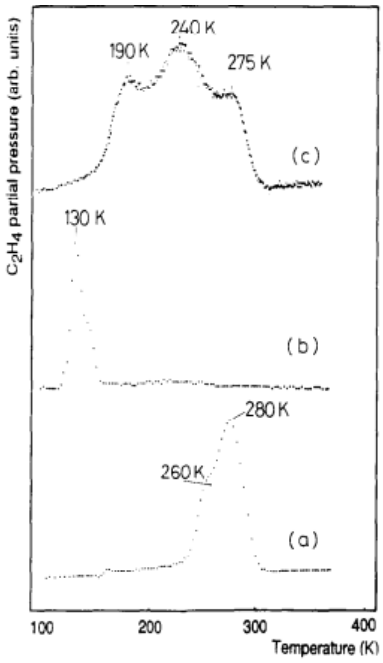

Figure 15. *Desorption spectra of molecular ethylene: (a) on bare Pt(111); (b) on 0.205 ML Cs-precovered Pt(111); (c) on 0.25 ML 0-precovered Pt(111).*

UPS experiments

Bare Pt(111) surface at low temperature

For UPS data, in order to identify the molecular orbitals coming from ethylene without opening the double bond, experiments have been performed at low temperatures (37 K) where multilayer growth is possible. The comparative analysis of the multilayer, the monolayer and gas phase spectra shows that the double bond is preserved at this temperature.

Figures 16b-16d show the formation of the first layer at 37 K and the subsequent growth of the ethylene multilayer (Figures 16e-16f). The transition between the monolayer and the multilayer is well characterized by an abrupt modification of the behavior of the work function change (Figure 16): the work function is significantly decreasing (-1.4 eV) during the formation of the monolayer and nearly constant afterwards. Apart from differences in relative intensities and positions, the spectrum of the first layer resembles that of the multilayer, although the π_{C-C} molecular orbital cannot be extracted from the d-band of the metal. This shows that the double bond is preserved at this temperature. However, annealing at 57 and 300 K leads to drastic changes correlated first to the transformation into a di-σ species and later on to conversion into ethylidyne [64].

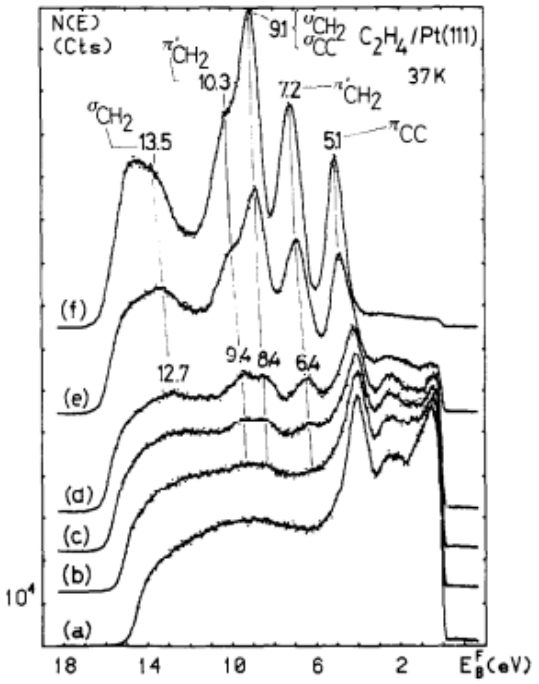

Figure 16. *Ethylene adsorption at 37 K on a bare Pt(111) surface: UP He1 spectra: (a) clean surface; (b) 0.3 ML C_2H_4; (c) 0.6 ML C_2H_4; (d) 1 ML C_2H_4; (e) 5 layers C_2H_4. (f) 10 layers C_2H_4.*

Bare, K- and Cs-precovered surfaces at 95 K

At 95 K, UP spectra of Figure 17 show clearly the difference in UP spectra between di-σ-bonded ethylene (Figure 17 b) formed on bare Pt(111) and π-bonded ethylene obtained on a K-precovered surface (Figure 17d). The potassium coverage was chosen in order to obtain the minimum work function and the maximum amount of π-bonded ethylene [67].

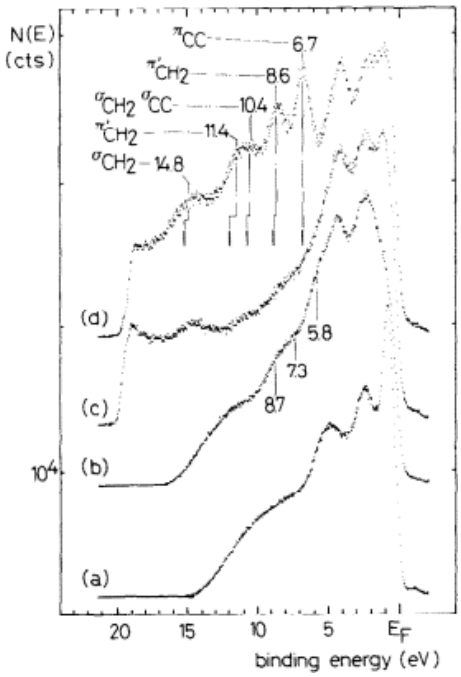

Figure 17. *Ethylene adsorption at 95 K: UP He I spectra (a) clear surface; (b) clear surface + ethylene saturation; (c) K precovered surface (0.17 ML); (d) ethylene saturation onto (c); the energy separations between the UP features are compared to those from the multilayer (Figure 16); the low lying orbitals having been aligned.*

A comparison is made in this figure with the orbitals derived from the multilayer. A shift of 1.6 eV has been used to adjust the two low-lying orbitals at the same energy. Curve 16c shows that when the work function decreases with deposition of potassium, a new feature appears at about 15 eV. No impurity could be detected using AES. Since neither the intensity of this feature nor its energy position are θ_K dependent, it has been attributed to the platinum substrate. However, in a difference spectrum between curves 16d and 16c, whatever the attenuation of the K-covered surface is, a residual peak appears at 14.8 eV which is due to ethylene adsorption. It has also been quoted in Figure 17.

The spectra analysis stands for a progressive conversion of adsorption mode with alkali coverage (Figure 18), leading to the maximum amount of π -bonded ethylene [67] at about 0.17 ML at minimum work function of the surface. An equivalent behavior is observed for the surface precoverage with Cs. Besides, an overall shift of all orbitals with potassium coverage without serious changes in the spacings between the orbitals is recorded [38, 39].

In order to check the reality of the shift of ethylene orbitals, additional experiments have been performed with variable amounts of potassium. They are shown in Figure 18. Even at relatively low K coverages, the characteristic orbitals of π-bonded ethylene can be clearly seen, (see the spectrum of Figure 18a). Figure 18 shows a global shift of all orbitals with potassium coverage without serious changes in the spacings between the orbitals.

In the case of Cs-precovered surfaces, previous results [64] have shown dramatic changes in the UP spectra with variable Cs coverages. The conversion of the di-σ-bonded species into

the π-bonded species could be easily observed, especially at a cesium coverage approaching that of the minimum of work function. However, π-bonded ethylene could be characterized by two orbitals only. They were attributed to π_{C-C} and π'_{CH_2}, the other low-lying orbitals being believed to be obscured by the presence of the Cs5p bands (see discussion below).

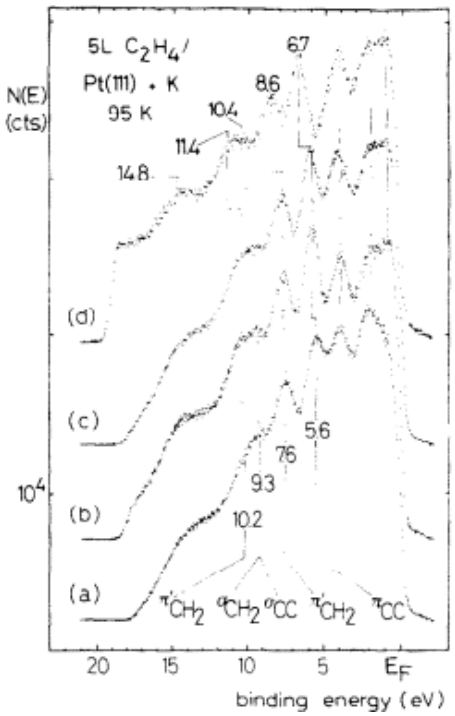

Figure 18. *Ethylene adsorption at 95 K in the presence of potassium: UP HeI spectra at various coverages: (a)* $\theta_K = 0.048\ ML$ *, (b)* $\theta_K = 0.075\ ML$*, (c)* $\theta_K = 0.1\ ML$ *and (d)* $\theta_K = 0.17\ ML$.

Discussion

Molecular adsorption of unsaturated hydrocarbons can be described in terms of distortions with respect to the free molecule [45, 69]. By analogy with previous works [48, 69, 70] we mean by di-σ bonded and π-bonded species, ethylene molecules for which the C=C double bond has strongly or mildly been disturbed, respectively. On bare Pt(111), at temperatures ranging between 90 and 250 K, vibrational spectroscopy [48, 69, 70] or calculations of the ionization potentials [69] and comparison with the UP spectrum support the idea that adsorbed C_2H_4 is reasonably described on the basis of an sp^3 hybridization and a sizeable disturbance of the angles and distances (C-C distance = 0.149 [69] or 0.152 nm, HCC angle = 110° or 114° [69] and HCH angle = 108° or 112° [69]), to be compared to the geometry of the free molecule (0.134 nm, 120° and 120°). If a "twist", ϕ, is introduced [69], this sp^3 character is kept as shown by the new set of values (C-C distance = 0.149 nm, HCC angle = 107°, HCH angle = 105° and $\phi = 29°$). The "di-σ" label is justified in this way, even if the molecule has retained part of its double-bond character as concluded from a XANES study [54]. "π-bonded" deuterated ethylene molecules found on K/Pt(111) and O/Pt(111) surfaces are characterized by vibrational stretch frequencies of the C-C bond (1495 and 1440 cm^{-1}) and of the C-D bond (2280 and 2230 cm^{-1}) [48, 67] close to the values of gaseous deuterated ethylene (1515 and 2251 cm^{-1}) [71]. The $\pi\sigma$ model developed by Stuve and Madix [22] leads to values of the $\pi\sigma$ parameter (which combines the percentage shift to lower frequency upon adsorption of both the C-C mode and the in-plane scissor CH_2 mode) equal to 0.04 and 0.38, respectively, while its value is 0.97 for the di-σ species.

The π-bonded C_2H_4 molecules

The multilayer formed below 52 K appears to be a good internal standard for "π-ethylene" without distortion: the energy level spacings of its UPS spectrum do not differ from those of the gas phase [72] within experimental errors (± 0.1). The monolayer obtained at 37 K gives almost the same spacings (see Figure 16; the orbitals are labelled following Jorgensen and Salem [73]) to the exception of the π_{C-C} orbital whose position is unknown (mixed with the d-band of the metal). It shows that adsorption leads to minor distortions, if any.

The π-ethylene molecules formed in the presence of alkali metals [64, 67] are mildly bonded to the Pt(111) surface as indicated by their desorption temperature. Under the influence of oxygen atoms, the bonding is clearly stronger, as indicated by a higher desorption temperature [38, 48].

Windham et al. [67] have shown, using HREELS, that increasing potassium coverages lead on Pt(111) to the appearance of π-bonded species at the expense of the di-σ ones. They also found that in the coverage range under investigation (0.066-0.264 K atomic ratio), the position of loss peaks for both species remained constant throughout, in the specular direction (dipole active losses) and off-specular (impact-scattering losses). They reached the important conclusion that *there was no change in the adsorption geometry for either species with increasing potassium coverage.* Furthermore, they show in Figure 9 of ref. [67] a UP spectrum of π -ethylene (at a potassium coverage equal to 0.165) where they assigned the two major peaks seen at 6.6 and 8.7 eV to π'_{CH_2} and σ_{C-C,CH_2} respectively.

The UP spectra in discussion (see Figure 17 and Figure 18) indicate that the molecular orbitals characteristic of π-ethylene shift with potassium coverage while the spacings between the orbitals remain almost unchanged. *The constancy of the spacings is in agreement with the absence of changes of the adsorption geometry* [67]. In Figure 17, when they are compared with those of the multilayer, they agree quite well after a shift of 1.6 eV. This means [69] that the molecule is almost *undistorted,* compared to the multilayer, taken as a reference. Compared to the monolayer (where the spacing between the π_{C-C} orbital and the π'_{CH_2} have been taken equal to that of the multilayer), the agreement is even better.

Knowing that the adsorption geometry is kept, the location and the spacings of the orbitals as well as their common shift with potassium coverage, lead us to propose a coherent attribution of the orbitals, shown in Figures 16-18, at variance with the one made by Windham et al. [67]. It shows that the π -bonded species formed at a potassium coverage corresponding to the minimum work function has its orbitals shifted by 2 eV or more as compared to the orbitals of the

monolayer obtained at 37 K. However, the spacings between the two π'_{CH_2} orbitals and the σ_{C-C,CH_2} orbital are systematically lower than those of the multilayer (gas phase) or the low temperature monolayer. Using the tables of ref. [69], it can be deduced qualitatively that such a behavior is only compatible with a slight "twist" of the adsorbed ethylene.

A similar behavior has been observed on the ethylene/Pt(111) + Cs system. There is no doubt about the formation of π- bonded ethylene on Cs-covered Pt(111) surfaces and its existence as a unique species for cesium coverages close to those corresponding to the minimum of the work function. It is demonstrated by the desorption temperature of ethylene (130 K see Figure 15) which is analogous to the desorption temperature of ethylene in the presence of potassium on the same surface [67]. In these conditions, the two orbitals due to the π-bonded ethylene in the UP spectra recorded from the C_2H_4/Pt(111) + Cs system (see Figure 19) were assigned [64] to the π_{C-C} (6.1 eV) and the π'_{CH_2} (8.2 eV) orbitals. We have assumed that the binding energy of these levels should be shifted towards higher binding energy with respect to those of the low temperature monolayer. This conclusion has now gained consistency as the previously assumed binding-energy shift has been directly observed on the qualitatively similar ethylene/Pt(111) + K system.

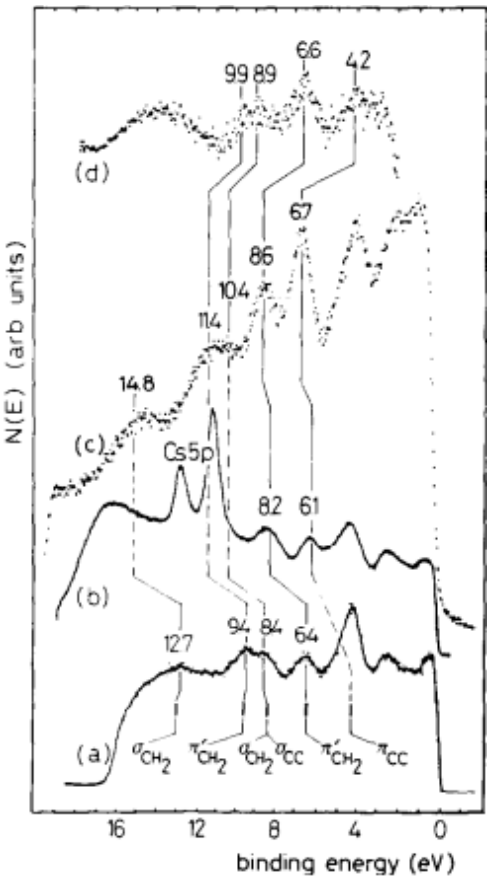

Figure 19. *UPS He1 spectra of π-bonded ethylene (as in Figure 17, the UP spectrum of the monolayer is used as a reference): (a) bare Pt(111) at 37 K: 1 ML C_2H_4, (b) 0.205 ML Cs-precovered Pt(111) at 95 K + C_2H_4 saturation; (c) 0.17 ML K-precovered Pt(111) at 95 K + C_2H_4 saturation; (d) 0.25 ML O-precovered Pt(111) at 95 K + C_2H_4 saturation*

6.2. Connection with Theoretical Models and Other Experimental Results

The almost undistorted π-C_2H_4 molecule seen on the K-precovered Pt(111) surface has been described by Windham et al. [67] in terms of the Chatt and Duncanson model [20]. They reached the conclusion that potassium inhibits the σ-donation of electrons from the C_2H_4 molecule to the surface (the same conclusion can be derived from the effect of the electrostatic potential induced by potassium [26]), meanwhile the backbonding from the d-band into the ethylene π^* orbital plays a minor role. However, although this model clearly accounts for the nature of bonding on the alkali-covered platinum surface, it does not explain so far the valence-band binding-energy shift recorded for the π-bonded C_2H_4 molecule when going from the clean (37 K) to the K(Cs)- covered Pt(111) surface.

The behaviour of ethylene on the K-covered platinum surface differs very much from that of CO on alkali metal-precovered surfaces. Many results evidence substantial changes in the C-O, and the C-metal bonds as well as, very often, direct alkali metal-CO interactions (Bonzel [74] for a review). In those conditions, the UP spectra of the CO molecules show complex combinations of shifts [74] which contrast with the wholly shifted spectra of C_2H_4/Pt(111) + K (Figure 18). The case of benzene on the K-covered Pt(111) surface is qualitatively more similar to our findings, since the two orbitals (assigned respectively to e_{1g} and to a combination of $A_{2u}(\pi)$ and σ-type orbitals) are shifted towards higher binding energy [75]. However, the shifts then recorded (< 1 eV) are lower than those observed in the present discussion. Meanwhile some orbitals are almost unshifted. Wandelt has proposed that the atomic levels of physisorbed atoms and particularly xenon follow the local work function [76]. The xenon atom is big enough to have its centre outside the surface potential barrier. The binding energies of its electronic levels are referred to the vacuum level [77] in such a way that their shifts mostly picture the variations of the local work function. In these conditions, strong shifts towards higher binding energies have been observed for the xenon levels on various surfaces, in the presence of potassium [78-82]. In the case of the isolated alkali adatoms (at very low K coverage), the shift experienced by the Xe5p levels relative to the potassium-free surface [78] fits quite well with the calculated variation of the electrostatic potential surrounding a potassium atom on a jellium surface [25]. This is in essence quite close to the ideas of Wimmer et al. [83] who have calculated how the valence levels of the CO molecule adsorbed on the Ni(100) surface could be perturbed by the modification of the electrostatic potential in the surface layer following the adjunction of potassium (neglecting overlap of orbitals); they have found huge shifts of the valence levels toward higher binding energies.

The valence-level binding-energy shifts associated with the loosely bonded π-C_2H_4 adsorbed in the presence of K (Cs) on the platinum surface (along with the work function changes

recorded in the same conditions) are summarized in Table 4 (It is only reported the binding energy of the π'_{CH_2} orbital, as representative of the whole spectrum). The electrostatic potential surrounding a polarized alkali adatom is a function of the distance from the surface [25]. Following Lang et al. [25], the onset of this disturbance is at about 0.1 nm and its maximum is about 0.3 nm for K. It is probably further away for Cs since this distance increases with the atomic size. Therefore, as the C_2H_4-Pt distance has been estimated as 0.18-0.19 nm [84] for weakly bonded species, the likely position of a π-bonded ethylene molecule is within the zone of disturbance of the alkali adatom but below the maximum of disturbance. Consistently, the valence-level binding energy shifts are seen to be only a fraction of the work function changes induced by the potassium and cesium, namely ranging between 0.4 and 0.6 of that change. Furthermore, at the alkali metal coverages corresponding to the respective minima of the work functions, the K-induced shift (2 eV or more as compared to the low temperature monolayer at $\theta_K = 0.17$) is higher than the Cs-induced shift (1.8 eV) which again follows the trend indicated by the value of the work function change. On clean metals (Ag(110), Cu foil, Fe foil and Ni(111)), Kelemen et al. [84] have found a shift of the second highest occupied level in π-bonded ethylene (π'_{CH_2}). Their figure 2 indicates a level shift equal to 0.66 of the work function change, from metal to metal, a result in agreement with the various electrostatic models described above and the results discussed here on alkali-covered Pt(111).

In conclusion, the formation of π-bonded species on alkali metal-precovered platinum agrees well with different models: donation and back-donation [67] and electrostatic interactions [25, 83]. They both predict a low adsorption energy in the presence of alkali metal adatoms. Therefore, the molecule is, in that case, almost undistorted compared to the gas phase molecule. But the effect of the electrostatic field in the vicinity of the polarized alkali adatom [25, 83], leads to an overall shift of the molecular orbitals of ethylene with alkali coverage.

Table 4. *Binding energies of the π'_{CH_2} orbital of the π-bonded C_2H_4 (BE π'_{CH_2}), shifts of these binding energies with respect to the bare Pt(111) surface (BE shift/bare surface), work function changes with respect to the bare surface ($\Delta\varphi$ - these values corresponding to the deposition of the alkali metal only) and the ratio $|\Delta\varphi / shift|$ for the C_2H_4/Pt(111) + K and C_2H_4/Pt(111) + Cs systems; various K coverages (corresponding to Figure 18) are given; the cesium coverage considered corresponds to the minimum of the work function.*

	Bare surface	C_2H_4/Pt(111)+K				C_2H_4/Pt(111)+Cs
		$\theta_{K=0.048\ ML}$	$\theta_{K=0.075\ ML}$	$\theta_{K=0.1\ ML}$	$\theta_{K=0.17\ ML}$	at φ_{min}
BE π'_{CH_2}	6+.4	7.6	7.8	8.1	8.6	8.2
BE shift/bare surface	-	1.2	1.4	1.6	2.2	1.8
$\Delta\varphi$	-	-2.05	-2.97	-4.0	-4.7	-4.25
$\lvert\Delta\varphi / shift\rvert$	-	0.6	0.47	0.4	0.46	0.42

7. Conclusive Discussion

All the preceding leads to conclude that the charge transfer TM-C in CNTs may be lowered by use of TM catalyst promotion by electropositive alkali metal atoms. The promotion of TM catalysts by electropositive atoms in the growth of CNTs by DC HF CCVD should lead to CNTs in what we denoted the bonding STATE2, with graphene sheets carbon weakly interacting with the TM particles. Thus leading to a lower charge transfer TM-C, either at the tip or along the sidewall shells. The grown CNTs may be less distorted, presenting minor defects and being of best quality, compared to those obtained without promotion (STATE1). These CNTs should have better properties and performances and allow easier purification conditions. That growth method may have implications in the defect industry and hydrogen storage, as well. These hypothesis and projections should be checked experimentally.

References

[1] Iijima, S. (1991) Helical Microtubules of Graphitic Carbon. *Nature*, 354, 56-58. http://dx.doi.org/10.1038/354056a0

[2] Melechko A V, Merkulov V I, MacKnight T E, Guillorn M A, Klein K L, Lowndes D H and Simpson M L, 2005, *J. Appl. Phys.* 97 041301.

[3] Groening, O.; Kuttel, O. M.; Emmenegger, C.; Groening, P. and Schlapbach, L. (1999) Field Emission Properties of Carbon Nanotubes. *Journal of Vacuum Science & Technology B: Microelectronics and Nanometer Structures*, 18, 665. http://dx.doi.org/10.1116/1.591258

[4] Wei, Y., Xie, C., Dean, K. A. and Coll, B. F. (2001) Stability of Carbon Nanotubes under Electric Field Studied by Scanning Electron Microscopy. *Applied Physics Letters*, 79, 4527-4529. http://dx.doi.org/10.1063/1.1429300

[5] Mane Mane, J., Thiodjio Sendja, B., Eba Medjo, R. (2015). Charge Transfer Transition Metal-Carbon at the Tips of CCVD Carbon Nanotubes Within the DCD Model. Journal of Materials Sciences and Applications, 1 (5): 239-255. (http://www.aascit.org/journal/jmsa)

[6] Chiou, J. W., Yueh, C. L., Jan, J. C., Tsai, H. M., Pong, W. F., *et al.,* (2002), Electronic Structure of the Carbon Nanotube Tips Studied by X-Ray-Absorption Spectroscopy and Scanning Photoelectron Microscopy, *Applied Physics Letters*, 81, 4189. http://dx.doi.org/10.1063/1.1523152

[7] Rosenberg, R. A., Love, P. J. and Rehn, V. (1986) Polarisation-Dependant Near-Edge X-Ray-Absorption Fine Structure of Graphite, *Physical Review B*, 33, 4034-4037. http://dx.doi.org/10.1103/PhysRevB.33.4034

[8] Mane Mane J., Le Normand F., Eba Medjo R., Cojocaru C. S., Ersen O., Senger A., Laffon C., Thiodjio Sendja B., Mbane Biouele C., Ben-Bolie G. H., Owono Ateba P., Parent P., Alignment of Vertically Grown Carbon Nanostructures Studied by X-Ray Absorption Spectroscopy, *Materials Sciences and Applications, 2014, 5, 966-983.*

[9] Eba Medjo R., Mane Mane J., Thiodjio Sendja B., XANES and Complementary Microscopy Studies of Carbon Nanostructure, LAP LAMBERT Academic Publishing (2015-02-02) - ISBN-978-3-659-66458-8.

[10] Comelli, G., Stohr, J., Jark, W. and Pate, B. B. (1988) Extended X-Ray-Absorption Fine-Structure Studies of Diamond and Graphite. *Physical Review B*, 37, 4383-4389. http://dx.doi.org/10.1103/PhysRevB.37.4383

[11] Fayette, L., Marcus, B., Mermoux, M., Tourillon, G., Parent, P., Laffon, K. and Le Normand, F. (1998) Local Order in CVD Diamond Films: Comparative Raman, X-Ray-Diffraction and X-Ray-Absorption Near-Edge Studies, *Physical Review B*, 57, 14123-14132. http://dx.doi.org/10.1103/Phys. Rev. B., 57.14123.

[12] Mubumbila, N., Bouchet-Favre, B., Godon, C., Marhic, C., Angleraud, B., Tessier, P. Y. and Minea, T. (2004) EELS and NEXAFS Structural Investigations on the Effects of the Nitrogen Incorporation in a-CN*x* Films Deposited by R. F. Magnetron Sputtering. *Diamond and Related Materials*, 13, 1433-1436. http://dx.doi.org/10.1016/j.diamond.2003.11.055

[13] Coffman, F. L., Cao, R., Pianetta, P. A., Kapoor, S., Kelly, M. and Terminello, L. J. (1996) Near-Edge X-Ray Absorption of Carbon Materials for Determining Bond Hybridization in Mixed sp2/sp3 Bonded Materials., *Applied Physics Letters*, 69, 568-570. http://dx.doi.org/10.1063/1.117789

[14] Enouz, S., Bantignies, J. L., Babaa, M. R., Alvarez, L., Parent, P., Le Normand, F., Stéphan, O., Poncharal, P., Loiseau, A. and Doyle, B. P. (2007) Spectroscopic Study of Nitrogen Doping of Multi-Walled Carbon Nanotubes. *Journal of Nanoscience and Nanotechnology*, 7, 3524-3527. http://dx.doi.org/10.1166/jnn.2007.839

[15] Eba Medjo R., Thiodjio Sendja B., Mane Mane J. and Owono Ateba P., "A Study of Carbon Nanotube Contamination by XANES Spectroscopy," *Physica Scripta*, Vol. 80, No. 4, 2009, Article ID: 045601.

[16] Banerjee, S., Hemraj-Benny, T., Sambavisan, S., Fischer, D. A., Misewich, J. A. and Wong, S. S. (2005) Near-Edge X-Ray Absorption Fine Structure Investigations of Order in Carbon Nanotube-Based Systems. *The Journal of Physical Chemistry B*, 109, 8489-8495., http://dx.doi.org/10.1021/jp047408t

[17] Mane Mane, J., Thiodjio Sendja, B., Eba Medjo, R., (2015), Contribution of Carbon Nanotubes Cap to XAS Signal, *Journal of Materials Sciences and Applications*, 1 (5): 195-220. (http://www.aascit.org/journal/jmsa)

[18] Mane Mane, PhD. Thesis in Material Science and Engineering, 1993, The University of Nancy I, Nancy, France.

[19] Dewar, M. Bull. Soc. Chim. Fr. 1951, 18, C79.

[20] Chatt, J. and Duncanson, L. A. 1953 *Olefin co-ordination compounds. Part III. Infra-red spectra and structure: attempted preparation of acetylene complexes,* J. Am. Chem. Soc., 75 2939 doi: 10.1039/JR9530002939.

[21] Stuve, E. M.; Madix, R. J.; Brundle, C. R., Surf. Sci., 1985, 152/153, 532.

[22] Stuve, E. M.; Madix, R. J., J. Phys. Chem., 1985, 89, 3183.

[23] Dravid, V. P., Lin, X., Wang, Y., Wang, X. K., Yee, A., Ketterson, J. B. and Chang, R. P. H. (1993) Buckytubes and Derivatives: Their Growth and Implications for Buckyball Formation. *Science*, 259, 1601-1602.

[24] Eba Medjo R. and C. N. Synthesis, "Carbon Nanotubes Applications on Electron Devices," In: J. M. Marulanda, Ed., *Carbon Nanotubes Applications on Electron Devices*, InTech, 2011, pp. 4-36. http://www.intechopen.com/books/carbon-nanotubes-applications-on-electron-devices/carbon-nanotube-synthesis

[25] Lang, N. D., Holloway S. and NØrskov, J. H. (1985) Surf. Sci. 150 24.

[26] NØrskov, J. K., Holloway, S. and Lang, N. D. (1985) J. Vac. Sci. Technol. A 3 1668.

[27] Kroto H. W., Heath J. R., O'Brien S. C., Curl R. F. and Smalley R. E., "C60: Buckminsterfullerene," *Nature*, Vol. 318, No. 6042, 1985, pp. 162-163. http://dx.doi.org/10.1038/318162a0

[28] Eba Medjo R., Thiodjio Sendja B. and Mane J., Curvature, hybridization and contamination of carbon nanostructures analysis using electron microscopy and XANES spectroscopy, *Materials Sciences and Applications, 2014, 5, 95-103.*

[29] Martinez A. and Yamashita S., "Carbon Nanotube-Based Photonic Devices: Applications in Nonlinear Optics," In: J. M. Marulanda, Ed., *Carbon Nanotubes Applications on Electron Devices*, InTech, 2011, pp. 367-386. http://www.intechopen.com/books/carbon-nanotubesapplications-on-electron-devices/carbon-nanotube-based-photonic-devices-applications-in-nonlinear-optics

[30] Dresselhaus, M. S., Dresselhaus, G. and Avouris, P. (2001) Carbon Nanotubes: Synthesis, Structure, Properties and Applications. Springer, Berlin, 29. http://dx.doi.org/10.1007/3-540-39947-X

[31] Mane Mane J., Cojocaru C. S., Barbier A., Deville J. P., Jean B., Metzger T. H., Thiodjio Sendja B. and Le Normand F., GISAXS study of the alignment of oriented carbon nanotubes grown on plain SiO_2/Si(100) substrates by a catalytically enhanced CVD process, *Phys. Stat. Sol. (a), vol. 204, N° 12, pp. 4209-4229 (2007) / DOI 10.1002/pssa. 200723201.*

[32] Chatt J., Duncanson L. A., Venanzi L. M., J. Chem. Soc., 1955, 4456-4460 doi: 10.1039/JR9550004456.

[33] Cojocaru, C. S., Senger, A. and Le Normand, F. (2006) A Nucleation and Growth Model of Vertically-Oriented Carbon Nanofibers or Nanotubes by Plasma-Enhanced Catalytic Chemical Vapor Deposition, *Journal of Nanoscience and Nanotechnology*, 6, 1331-1338. http://dx.doi.org/10.1166/jnn.2006.144

[34] Costel Sorin Cojocaru, Ph.D Thesis, The University Louis Pasteur, Strasbourg I, Strasbourg, France, 2003.

[35] Suzuki, S., Watanabe, Y., Kiyokura, T., Nath, K. G., Ogino, T., Heun, S., Zhu, W., Bower, C. and Zhou, O., (2001), Electronic Structure at Carbon Nanotube Tips Studied by Photoemission Spectroscopy. *Physical Review B*, 63, 1-7.

[36] Suzuki, S., Watanabe, Y., Ogino, T., Heun, S., Gregoratti, L., Barinov, A., Kaulich, B., Kiskinova, M., Zhu, W., Bower, C. and Zhou, O. (2002) Electronic Structure of Carbon Nanotubes Studied by Photoelectron Spectromicroscopy, *Physical Review B*, 66, 1-4.

[37] Kroto, H. W., The stability of Fullerene Cn (n= 24, 28, 32, 50, 60 and 70), Nature, 329, 529, 1987.

[38] Cassuto, A., Mane Mane, Hugenschmidt, M., Dolle, P. and Jupille J. (1990) The effect of K, Cs and 0 atoms on ethylene adsorption on the Pt(111) surface, *Surface Science*, 237 63-71.

[39] Cassuto, A., Mane Mane., Kronneberg, V. and J. Jupille. (1991) Molecular orbital shifts of T-bonded ethylene adsorbed on Pt(111) in the presence of potassium atoms, *Surface Science*, 251/252 1133-1137.

[40] Cassuto, A., Mane Mane., and J. Jupille. (1991) Ethylene monolayer and multilayer on Pt(111.) below 52 K: determination of bond lengths by near-edge X-ray fine structure, *Surface Science*, 249 8-14.

[41] Cassuto, A., Schmidt, S. and Mane Mane. (1993) The interaction of potassium submonolayers adsorbed on Pt(111) with oxygen and the adsorption of ethylene on the resulting modified surfaces: a TDS and UPS study, *Surface Science*, 284 273-280.

[42] Cassuto, A., Mane Mane., Tourillon, G., Parent, P., and Jupille, J. (1993) Compared bonding geometries of C_2H_4 and C3H6 on K-covered Pt(111) surfaces, *Surface Science*, 287/288 460-464.

[43] Kesmodel, L. L., Dubois, L. H. and. Somorjai, G. A. (1978) *Chem. Phys. Lett.* 56 267.

[44] Kesmodel, L. L., Dubois, L. H. and. Somorjai, G. A. (1979) *J. Chem. Phys.* 70 2180.

[45] Demuth, J. E., (1979) *Surf. Sci*. 80 367.

[46] Canning, N. D. S., Baker, M. D. and Chesters, M. A. (1981) *Surf. Sc*i. 111 441.

[47] Baro, A. M. and Ibach, H. (1981) *J. Chem. Phys*. 74 4194.

[48] Steininger, H., Ibach, H. and Lehwald, S. (1982) *Surf. Sci.* 117 685.

[49] Salmeron, M. and. Somorjai, G. A (1982) *J. Phys. Chem.* 86 341.

[50] Albert, M. R., Sneddon, L. C., Eberhardt, W., Greuter, F., Gustafsson, T. and Plummer, W. (1982) *Surf. Sci*. 120 19.

[51] Freyer, N., Pirug, G. and Bonzel, H. P. (1983) *Surf. Sci*. 125 327.

[52] Creighton, J. R. and White, J. M. (1983) *Surf. Sci*. 129 327.

[53] Zaera, F. and Somorjai, G. A. (1984) *J. Am. Chem. Soc.* 106 2288.

[54] Koestner, R. J., Stöhr, J., Gland, J. L. and. Horseley, J. A. (1984) *Chem. Phys. Lett*. 105 332; Horseley, J. A., Stöhr, J. and Koestner, R. J. (1985) *J. Chem. Phys*. 83 3146.

[55] Creighton, J. R., Ogle, K. M. and White, J. M. (1984) *Surf. Sci.* 138 L137.

[56] Davis, SM., Zaera, F., Gordon, B. E. and Somorjai, G. A. (1985) *J. Catal.* 92 240.

[57] Godbey, D.. Zaera, F., Yeates R. and Somorjai, G. A. (1986) *Surf. Sci.* 167 150.

[58] Ogle, H. M., Creighton, J. R., Akhter, S. and White, J. M. (1986) *Surf. Sci.* 169 246.

[59] Yu, R. and Gustafsson, T. (1987) *Surf. Sci.* 182 L234.

[60] Malik, I. J., Brubaker, M. E., Moshin S. B. and Trenary, M. (1987) *J. Chem. Phys*. 87 5554.

[61] Zhou, X. L., Zhu, X. Y. and White, J. M. (1988) *Surf. Sci.* 193 387.

[62] Malik, I. J., Agrawai, V. K. and Trenary, M. (1988) *J. Chem. Phys.* 89 3861.

[63] Gland, J. L., Zaera, F., Fischer, P., Carr, R. and E. B. Kollin, (1988) *Chem. Phys. Lett.* 151 227.

[64] Hugenschmidt, M. B., Dolle, P., Jupille, J. and Cassuto, A. (1989) *J. Vac. Sci. Technol.* A 7 3312.

[65] Barteau, M. A., Broughton, J. Q. and Menzel, P. 1984 *Appl. Surf. Sci.* 19 92.

[66] Windham, R. G., Bartram, M. E. and Keel, B. E. (1987) *J. Vac. Sci. Technol. A* 5 457.

[67] Windham, R. G., Bartram, M. E. and Koel, B. E. (1988) *J. Phys. Chem.* 92 2862.

[68] Redhead, P. A. (1962) Vacuum 12 203.

[69] Felter, T. E. and Weinberg, W. H. (1981) Surf. Sci. 103 265.

[70] Ibach, H. and Lehwald, S. (1978) J. Vac. Sci. Technol. 15 407.

[71] Herzberg, G. (1945), Molecular Spectra and Molecular Structure, II. Infrared and Raman Spectra of Polyatomic Molecules (Van Nostrand-Reinhold, New York,) p. 326.

[72] Turner, D. W., Baker, C., Baker, A. D. and Brundle C. R. (1970) (Wiley-Interscience, New York) p. 179.

[73] Jorgensen W. L. and Salem, L. (1973) The Organic Chemist's Book of Orbitals (Academic Press, New York).

[74] Bonzel, H. P. (1988) Surf. Sci. Rep. 8 43.

[75] Kudo, M., Garfunkel, E. L. and Somorjai, G. A. (1985) J. Phys. Chem. 89 3207.

[76] Wandelt, K. (1984) J. Vac. Sci. Technol. A 2 802.

[77] Lang, N. D. and Williams, A. R. (1982) Phys. Rev. B 25 2940.

[78] Markert, K. and Wandelt, K. (1985) Surf. Sci. 159 24.

[79] Mullins, D. R. White, J. M. and Luftman, H. S. (1985) Surf. Sci. 160 70.

[80] Lee, J. Hanrahan, C. Arias, J. Martin, R. M. and Metiu, H. Surf. Sci. 161 (1985) L543.

[81] Onellion, M. and Erskine, J. L. (1986) Surf. Sci. 177 1983.

[82] Mullins, D. R., White, J. M. and Luftman, H. S. (1987) Surf. Sci. 167 39.

[83] Wimmer, E., Fu, C. L. and Freeman, A. J. (1985) Phys. Rev. Lett. 55 2618.

[84] Kelemen, S. R. and Fisher, T. E. (1981) Surf. Sci. 102 45.